Immunotherapy-activated T cells recruit and skew late-stage activated M1-like macrophages that are critical for therapeutic efficacy

Elsas, M.J. van; Middelburg, J.; Labrie, C.; Roelands, J.; Schaap, G.; Sluijter, M.; ... ; Burg, S.H. van der

Cancer Cell

Article

Immunotherapy-activated T cells recruit and skew late-stage activated M1-like macrophages that are critical for therapeutic efficacy

Graphical abstract

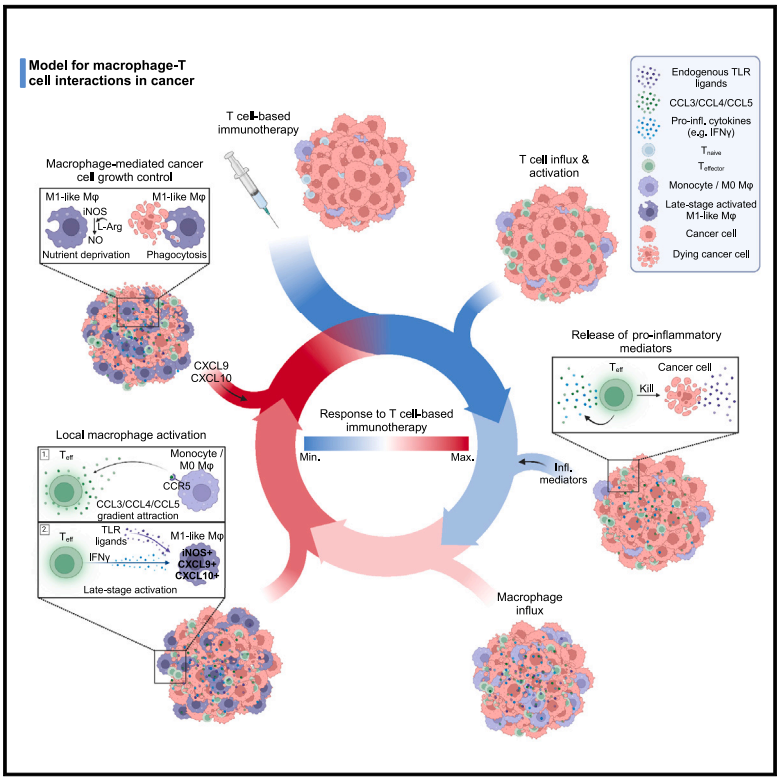

Authors

Marit J. van Elsas, Jim Middelburg, Camilla Labrie, ..., Noel F.C.C. de Miranda, Thorbald van Hall, Sjoerd H. van der Burg

Correspondence

shvdburg@lumc.nl

In brief

van Elsas et al. demonstrate that immunotherapy-induced intratumoral CD8$^+$ T cells attract macrophages into their close vicinity via CCR5-signaling and subsequently differentiate them toward a late-stage activated M1-like phenotype. These macrophages play a crucial role in effective tumor control in mouse models and are correlated to clinical responses in humans.

Highlights

- Immunotherapy-induced CD8$^+$ T cells summon macrophages via CCR5 signaling
- Activated T cells skew macrophages into late-stage activated M1-like macrophages
- Late-stage activated M1-like macrophages are critical for effective tumor control

van Elsas et al., 2024, Cancer Cell *42*, 1032–1050
June 10, 2024
https://doi.org/10.1016/j.ccell.2024.04.011

CellPress

CellPress
OPEN ACCESS

Cancer Cell

Article

Immunotherapy-activated T cells recruit and skew late-stage activated M1-like macrophages that are critical for therapeutic efficacy

Marit J. van Elsas,[1,6] Jim Middelburg,[1,6] Camilla Labrie,[1,7] Jessica Roelands,[2,7] Gaby Schaap,[1] Marjolein Sluijter,[1] Ruxandra Tonea,[3,4] Vitalijs Ovcinnikovs,[5] Katy Lloyd,[5] Janine Schuurman,[5] Samantha J. Riesenfeld,[4] Thomas F. Gajewski,[3] Noel F.C.C. de Miranda,[2] Thorbald van Hall,[1] and Sjoerd H. van der Burg[1,8,*]

[1]Department of Medical Oncology, Oncode Institute, Leiden University Medical Center, Leiden 2333ZA, the Netherlands
[2]Department of Pathology, Leiden University Medical Center, Leiden 2333ZA, the Netherlands
[3]Department of Pathology, University of Chicago, Chicago, IL 60637, USA
[4]Pritzker School of Molecular Engineering, Chicago, IL 60637, USA
[5]Genmab, Utrecht 3584CT, the Netherlands
[6]These authors contributed equally
[7]These authors contributed equally
[8]lead contact
*Correspondence: shvdburg@lumc.nl
https://doi.org/10.1016/j.ccell.2024.04.011

SUMMARY

Total tumor clearance through immunotherapy is associated with a fully coordinated innate and adaptive immune response, but knowledge on the exact contribution of each immune cell subset is limited. We show that therapy-induced intratumoral CD8$^+$ T cells recruited and skewed late-stage activated M1-like macrophages, which were critical for effective tumor control in two different murine models of cancer immunotherapy. The activated CD8$^+$ T cells summon these macrophages into the tumor and their close vicinity via CCR5 signaling. Exposure of non-polarized macrophages to activated T cell supernatant and tumor lysate recapitulates the late-stage activated and tumoricidal phenotype *in vitro*. The transcriptomic signature of these macrophages is also detected in a similar macrophage population present in human tumors and coincides with clinical response to immune checkpoint inhibitors. The requirement of a functional co-operation between CD8$^+$ T cells and effector macrophages for effective immunotherapy gives warning to combinations with broad macrophage-targeting strategies.

INTRODUCTION

Therapies that reinvigorate the body's own immune system to target tumor cells have resulted in remarkable response rates for many cancer types. Most of these therapies are focused on the T cell compartment. Therapeutic cancer vaccines are tools to induce or augment an anti-tumor response by facilitating the activation and tumor infiltration of effector T cells, while immune checkpoint inhibitors (ICIs) or CD3-engaging bispecific antibodies (CD3 bsAbs) utilize and sustain the effector function of T cells that are already present within the tumor microenvironment (TME). However, accumulating evidence suggests the need for a coordinated immune response to reach total tumor control, one that involves the action of innate immune cells, rather than relying on a strong T cell response alone.[1–3]

The immune contexture comprises the type, density, location, and functional orientation of all immune cells within the tumor and can be used as a prognostic score for survival or therapy response.[1,2] The role of CD8$^+$ T cells has been studied extensively, with studies consistently demonstrating their strong positive correlation with survival.[1] Nevertheless, other immune cells are also associated with improved overall survival rates and the response to immunotherapy, including natural killer (NK) and B cells, M1 macrophages, dendritic cells, T helper 1 cells, and, in some types of tumors, mast cells and eosinophils.[1] While these associations suggest a role for other immune cells beyond CD8$^+$ T cells, they do not formally demonstrate whether these cells contribute to tumor control or how they become engaged by different forms of immunotherapy.[4] While myeloid cells are generally known for their suppressive functions,[5] their help in the anti-tumor response is increasingly established,[6–8] whereas others indicate that exploitation of their tumoricidal function may also provide tumor control.[9–12] Additionally, the existing literature is mainly focused on the attraction of T cells by myeloid cells through the CXCL9/10-CXCR3 axis,[6,13] but their interaction can be reciprocal and other signaling pathways (i.e., CCR5, IL-12, or interferons) might also be of importance.[3,14–16] Therefore, we aim to clarify the exact contribution and mechanism of action

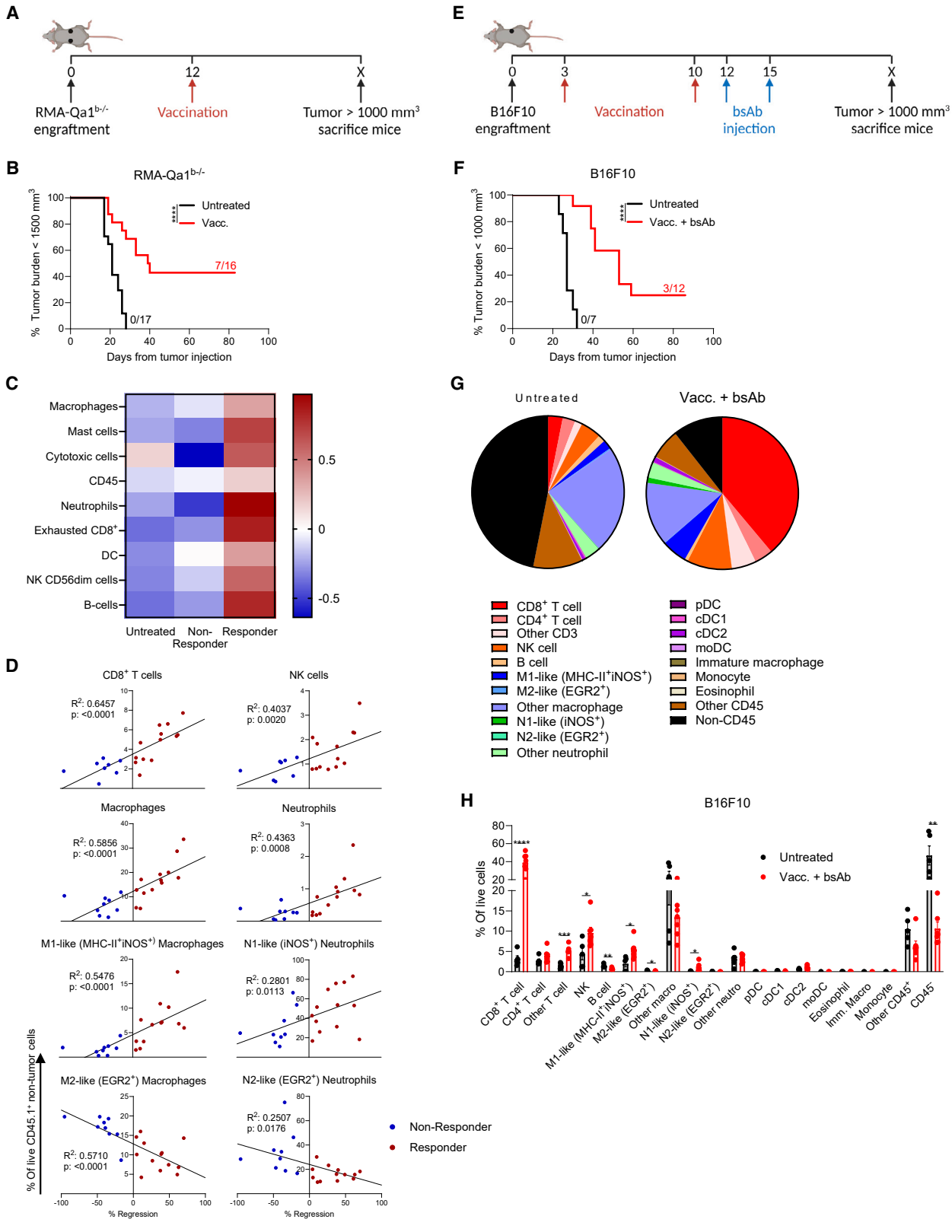

(legend on next page)

of each individual type of immune cell to tumor regressions following T cell-based immunotherapy.

In this study, we use two different T cell-based immunotherapies in murine models, both of which consist of therapeutic vaccination to obtain more intratumoral effector CD8$^+$ T cells, in combination with either ICI or CD3 bsAb, to determine the immune cell types crucial for effective therapeutic responses. Through comprehensive analyses of the TME and perturbation studies, we show that the tumor infiltration by both a population of pro-inflammatory M1-like macrophages and tumor-reactive CD8$^+$ T cells is of pivotal importance for tumor control. The intratumoral CD8$^+$ T cells recruit these macrophages into the tumor and attract them into their close vicinity via the CCR5 axis to activate them. Importantly, we confirm the presence of a similar population of late-stage activated M1-like macrophages in human tumors and demonstrate that their presence positively correlates with the response to ICI therapy.

RESULTS

Response to immunotherapy depends on CD8$^+$ T cells and macrophages

To identify immunological factors contributing to tumor regression induced by immunotherapy, we used the established Rauscher's murine leukemia virus-induced RMA-Qa1$^{b-/-}$ tumor model, treated with a tumor-specific therapeutic synthetic long peptide vaccination.[17,18] Vaccination resulted in significantly improved survival with complete clearance of some tumors, while other tumors did not respond at all (primary resistance), or relapsed after initial regressions (secondary resistance, Figures 1A, 1B, S1A, and S1B). Importantly, all treated mice displayed a substantial increase in intratumoral tumor-specific CD8$^+$ T cells (Figure S1C) and lack of response could not be corrected by a booster vaccination (Figure S1D). Analysis of the TME revealed that the frequencies of CD8$^+$ T cells, M1-like macrophages (defined as iNOS$^+$MHCII$^+$),[19] and immature macrophages were significantly increased after vaccination (Figures S1E–S1H). In comparison to other macrophages, these M1-like macrophages more often expressed PD-L1, SIRPα, CD86, and, in particular, CD11c, CXCL9, IL-12, and CD40. Similar to the other subset, they often expressed Ly6C and CD70 (Figure S1I). To analyze the response of tumors on a transcriptional level, mice with vaccine-induced regressing tumors (on day 19 of the experiment) were classified as "responders," whereas mice with non-regressing tumors at this time point were classified as "non-responders." At the transcriptomic level, tumors from non-responding mice did not significantly differ from their untreated counterparts (Figure S2A), whereas the tumors from responding mice were enriched in gene scores associated with the presence of inflammatory cell types (Figure 1C). These results were validated by flow cytometry, showing a significant positive correlation between response to immunotherapy and increased numbers of CD8$^+$ T cells, NK cells, macrophages, and neutrophils (Figure 1D). When the macrophage and neutrophil populations were split into the M1-like (iNOS$^+$MHCII$^+$)/N1-like (iNOS$^+$) and M2-/N2-like (EGR2$^+$) subpopulations,[12,19] a strong positive correlation between response to immunotherapy and M1/N1-like subsets was found, while their M2/N2-like counterparts correlated negatively with response (Figure 1D). CD4$^+$ T cells, B cells, or eosinophils showed no correlation with response (Figure S2B). The presence of inflammatory cells in the TME was accompanied by an increase in the expression of gene signatures involved in inflammation, including cytokine and interferon signaling pathway, thereby further strengthening the correlation between an active immune response and therapy outcome (Figure S2C).

To validate our findings, similar analyses were performed on B16F10 (B16) melanoma tumors, treated with a combination of CD3xTRP1 bispecific antibody (bsAb) and an imiquimod and IL-2-adjuvanted vaccine, to achieve T cell infiltration in the tumor and subsequent bsAb-mediated execution of T cell effector functions against the tumor, as previously described.[20] This combination therapy (Figure 1E) delayed tumor outgrowth and increased the number of surviving mice (Figures 1F and S2D). Similar to responding tumors in the RMA-Qa1$^{b-/-}$ model, the combination treatment of B16 tumors resulted in enhanced influx of CD8$^+$ T cells, NK cells, M1-like macrophages, and N1-like neutrophils, while the percentages of B cells, M2-like macrophages, and non-immune (CD45-negative) cells were decreased (Figures 1G and 1H). Based on the expression of several markers, tumor-infiltrating CD8$^+$ T cells, NK cells, macrophages, and neutrophils were more activated following immunotherapy (Figure S2E). The iNOS$^+$MHCII$^+$ M1-like macrophages in this tumor more often expressed CXCL9, IL-12, CD86, and PD-L1 (Figure S2F). Since these molecules were upregulated by the M1-like macrophages in both tumors, their increased expression characterizes this iNOS$^+$MHCII$^+$ M1-like macrophage population. Altogether, this shows that therapy responses positively correlated with the influx of activated CD8$^+$ T cells, NK cells, (M1-like) macrophages, and (N1-like) neutrophils in two distinct tumor therapy models.

The contribution of each effector cell type that showed a positive correlation with therapy response was studied by injecting depleting antibodies against CD8, NK1.1 (NK cells), CD115 (macrophages), and Ly6G (neutrophils) and monitoring tumor outgrowth (Figures 2A and 2B). Depletion of NK cells did not

Figure 1. Responders to two distinct immunotherapies have an immune-inflamed TME

(A) Treatment schedule and (B) Kaplan-Meier graph of mice bearing RMA-Qa1$^{b-/-}$ tumors.

(C) Scores for immune cell subsets in RMA-Qa1$^{b-/-}$ tumors from bulk transcriptomic analysis generated by nSolver software. Red, high relative expression; blue, low relative expression.

(D) Correlation between immune cell infiltrate as frequency of live CD45.1$^+$ (non-tumor) cells in RMA-Qa1$^{b-/-}$ tumors, and therapy response.

(E) Treatment schedule and (F) Kaplan-Meier graph of mice bearing B16F10 tumors.

(G and H) Immune infiltrate in B16F10 tumors out of total live cells represented as (G) pie charts or (H) bar graphs. Vacc., vaccination; Imm., immature. Data represented as mean (C, G) or mean ± SEM (H) for $n = 3$–4 (C) or $n = 5$–7 (G and H). Significance was calculated using Mantel-Cox log rank tests (B and F), simple linear regression (D), or unpaired two-sided t tests (H). Statistical significance is shown as * = $p < 0.05$, ** = $p < 0.01$, *** = $p < 0.001$, and **** = $p < 0.0001$. See also Figures S1 and S2.

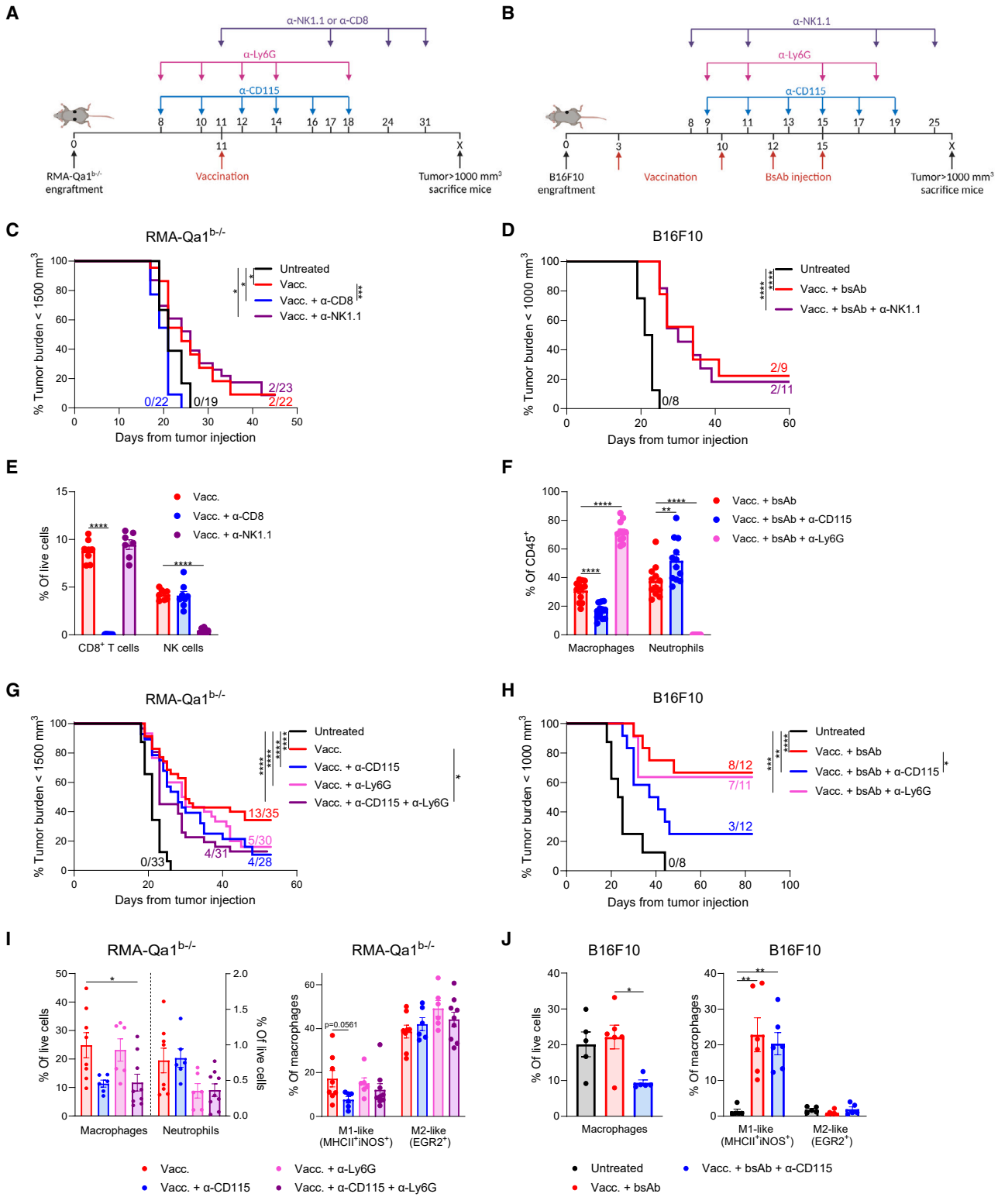

Figure 2. Macrophages are essential for therapeutic efficacy

Treatment schedule for mice receiving CD8, NK1.1, CD115, or Ly6G depleting antibodies, while bearing (A) RMA-Qa1$^{b-/-}$ or (B) B16F10 tumors. Kaplan-Meier survival graph for mice receiving CD8 or NK depleting antibodies, bearing (C) RMA-Qa1$^{b-/-}$ or (D) B16F10 tumors.

(E and F) Depletion efficiencies in blood on day 12. Kaplan-Meier survival graph for mice receiving CD115 or Ly6G depleting antibodies, bearing (G) RMA-Qa1$^{b-/-}$ or (H) B16F10 tumors.

(legend continued on next page)

impact the response to therapy in either model (Figures 2C–2E), while the therapeutic effect of vaccination against RMA-Qa1$^{b-/-}$ tumors was completely abolished when CD8$^+$ T cells were depleted (Figures 2C and 2E). The dependency on either CD8$^+$ or CD4$^+$ T cells for CD3 bsAb treatment in the B16 model has previously been demonstrated.[21] The response of RMA-Qa1$^{b-/-}$ tumors depended on both macrophages and neutrophils, as reflected by reduced survival following depletion of either population (Figures 2F and 2G). Depletion of both populations further impaired treatment outcome, hinting towards an additive effect for these two effector cell types. In the B16 model, survival was significantly decreased upon depletion of macrophages but not neutrophils (Figures 2F and 2H). Altogether, these results demonstrate that macrophages are required for potent tumor control in two different tumor models.

The impact of cell depletion could equally reflect the direct anti-tumor role of the targeted cell type or the downstream effects on other immune cells. To examine this, the TME of treated animals was extensively analyzed using spectral flow cytometry with over 50 markers. The strongly impaired therapeutic response after macrophage depletion with an α-CD115 antibody was associated with an approximately 50% reduction in macrophages in the TME of RMA-Qa1$^{b-/-}$ tumors (Figure 2I). In addition to overall reduction in macrophages, the MHCII$^+$iNOS$^+$ M1-like population was further decreased in RMA-Qa1$^{b-/-}$ tumors treated with α-CD115, but not when neutrophils were depleted by α-Ly6G (Figures 2I and S3A). In the B16 model, the total number of macrophages was also lower after α-CD115 (Figure 2J). As the M1-like macrophage subset (MHCII$^+$iNOS$^+$) was the dominant population over M2 macrophages, the depletion of macrophages in B16 tumors predominantly affected the total number of M1-like macrophages (Figures 2J and S3B). No other overt changes in immune cell composition were observed in both tumor models following macrophage depletion, nor when neutrophils were depleted in RMA-Qa1$^{b-/-}$ (Figures S3C and S3D). Importantly, the phenotype and effector function of intratumoral CD8$^+$ T cells was not affected by either macrophage or neutrophil depletion in both tumor models (Figures S3E and S3F). This indicates that the observed loss of therapy response was not due to alterations in the intratumoral CD8$^+$ T cell population, which are assumed to be the main effector cells in both therapies. Interestingly, the few neutrophils present in RMA-Qa1$^{b-/-}$ tumors (Figure 2I) lost their activated phenotype after macrophage depletion (Figure S3G), suggesting they are influenced by M1-like macrophages. Together, these findings imply a prominent role for macrophages as effector cells in tumor control in two T cell-based therapy models.

Activated intratumoral CD8$^+$ T cells are essential for the presence of M1-like macrophages

Next, we investigated if therapy-driven CD8$^+$ T cells dictated the numbers and phenotype of other immune cells in the TME. Opt-SNE embedding of myeloid cells (CD11b$^+$ and/or CD11c$^+$) from RMA-Qa1$^{b-/-}$ tumors of animals treated with and without CD8$^+$ T cell depletion allowed us to investigate changes in an unbiased manner. Depletion of CD8$^+$ T cells resulted in the complete ablation of RMA-metaclusters (RMCs) 11 and 19, while RMC17 strongly increased (Figures 3A–3C). Heatmap representation of lineage and phenotypic markers across different RMCs revealed these clusters to be macrophages (CD11b$^+$F4/80$^+$, Figure 3D). More specifically, RMC11 and 19 were found to be iNOS$^+$ M1-like macrophages (MHCII$^+$), while RMC17 included EGR2$^+$ SIRPα$^+$MHCII$^-$ M2-like macrophages.

Indeed, a complete absence of iNOS$^+$ macrophages is captured in the tSNE plot upon CD8$^+$ T cell depletion (Figure 3E). Besides this pronounced effect on iNOS$^+$ M1-like and EGR2$^+$ M2-like macrophages, depletion of CD8$^+$ T cells also resulted in a significant decrease in Ly6C$^+$ M1-like macrophages (RMC09), inflammatory eosinophils (RMC02), and dendritic cells (RMC14), while CD163$^+$ M2-like macrophages (RMC20 and RMC12), immature macrophages (RMC08), neutrophils (RMC03), and a subpopulation of MHCII$^+$ macrophages (RMC13) were increased (Figures 3B and 3D). Manual gating on flow cytometry data of RMA-Qa1$^{b-/-}$ tumors revealed that the efficient depletion of CD8$^+$ T cells was accompanied by a decrease in macrophages, CD4$^+$ T cells, and NK cells (Figures 3F and S4A), while no effect was seen on the activation status of neutrophils (Figure S4B). Furthermore, a change in myeloid cell markers was observed, shifting from a highly activated pro-inflammatory M1-like state (iNOS, MHCII, CD40, CD70, and Ly6C) to an anti-inflammatory M2-like state with increased EGR2 and Siglec-G expression (Figure S4C), emphasizing the impact of CD8$^+$ T cell-macrophage interactions.

In the B16 model, both CD8$^+$ and CD4$^+$ T cells were depleted, as CD3 bsAb therapy can act on both subsets.[21] Unsupervised opt-SNE embedding of myeloid cells (CD11b$^+$CD45$^+$) confirmed our findings in the RMA-Qa1$^{b-/-}$ model, as T cell depletion resulted in a reduction of iNOS$^+$ M1-like macrophage B16 metaclusters BMC02 and 05, whereas the augmented frequencies of BMC06, 10, 13, and 20 mainly represented M2-like macrophages expressing SIRPα and EGR2 and varying degrees of CD163 and Arg1 (Figures S4D–S4F). Manual gating of the flow cytometry data further revealed that depletion of CD8$^+$ and CD4$^+$ T cells coincided with a significant decrease in pDC and cDC1 cells and confirmed the decrease in iNOS$^+$ macrophages (Figures 3G, 3H, S4G, and S4H). In contrast to the RMA-Qa1$^{b-/-}$ tumor model, T cell depletion did not completely ablate the M1-like macrophages, which may be due to the presence of strongly activated NK cells (Figures 1G, 1H, and S2E), which may compensate for the loss of T cell-derived macrophage stimulating chemokines.[22]

In summary, the presence of therapy-activated T cells in the TME is responsible for the recruitment of M1-like macrophages. Moreover, the reduction in tumor response following CD115 depletion, despite sustained numbers and activation of lymphoid

(I) Intratumoral frequencies of macrophages and neutrophils and phenotype of macrophages in mice bearing RMA-Qa1$^{b-/-}$ tumors.
(J) Intratumoral frequency and phenotype of macrophages in mice bearing B16F10 tumors. Vacc., vaccination. Data represented as mean ± SEM for n = 7–8 (E), n = 11–12 (F), or n = 5–9 (I and J). Significance was calculated using Mantel-Cox log rank tests (C, D, G, and H), one-way ANOVA and Tukey post hoc tests comparing all treatment groups (E, F, and J), or one-way ANOVA and Dunnett post hoc tests compared to Vacc. (I). Statistical significance is shown as * = $p < 0.05$, ** = $p < 0.01$, *** = $p < 0.001$, and **** = $p < 0.0001$. See also Figure S3.

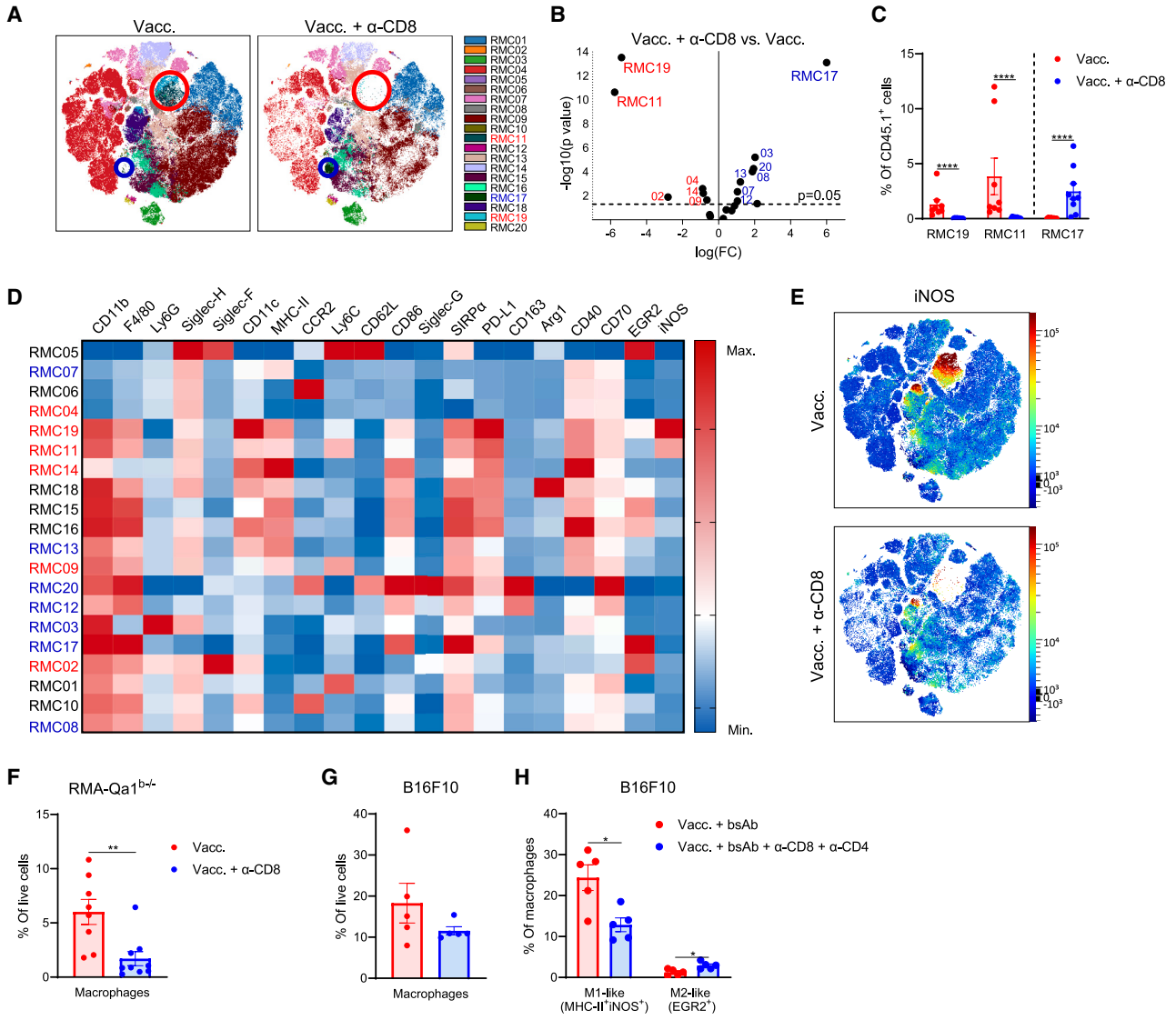

Figure 3. T cell depletion results in loss of iNOS$^+$ M1-like macrophages

(A–E) Unsupervised embedding of pre-gated CD11b$^+$/CD11c$^+$ myeloid cells in RMA-Qa1$^{b-/-}$ tumors shown as (A) metacluster overlay on opt-SNE, (B) metacluster distribution on a volcano plot, or (C) bar graph and (D) heatmap showing phenotypical marker expression for all metaclusters. (E) Expression of iNOS (mean fluorescence intensity) from pre-gated CD11b$^+$ and/or CD11c$^+$ cells. Frequency of intratumoral macrophages in (F) RMA-Qa1$^{b-/-}$ or (G) B16F10 tumors. Frequencies were normalized to B cells to correct for the loss of the major T cell populations. (H) Phenotype of macrophages in B16F10 tumors for indicated treatment groups. Data represented as mean (B, D) or mean ± SEM (C, F–H) for $n = 6$–9 (A–D, F), or $n = 5$–6 (G and H). Significance was calculated using edgeR test (B), or unpaired two-sided t tests (C, F–H). Statistical significance is shown as * = $p < 0.05$, ** = $p < 0.01$, *** = $p < 0.001$, and **** = $p < 0.0001$. See also Figure S4.

effector cells, strongly indicates a direct tumor-controlling effector function for M1-like macrophages.

T cells can augment M1-like macrophage polarization

To determine if CD8$^+$ T cells influenced the inflammatory state of intratumoral macrophages in a direct manner, bone-marrow-derived unstimulated and IFN-γ/LPS-polarized macrophages (BMDMs) were cultured in the presence of supernatant, isolated from CD8$^+$ T cells that were stimulated either with the cognate tumor antigen for RMA-Qa1$^{b-/-}$ (GagL peptide) or in a non-specific manner using CD3/CD28 dynabeads (Figure 4A). The presence of activated T cell supernatant skewed naive BMDMs towards a pro-inflammatory M1-like phenotype, reflected by an increased expression of iNOS, MHCII, CD86, and PD-L1 (Figures 4B, S5A, and S5B). When we interrogated the additive effect of activated T cell supernatant on M1 BMDMs, the expression of iNOS in particular showed a marked increase (Figure 4B). We confirmed that intratumoral T cells possessed this polarizing capacity by isolating these CD8$^+$ T cells from combination therapy-treated B16 tumors and subjecting them to *in vitro* reactivation using B16 tumor cells and bsAb to mimic T cell activation in the tumor. Subsequently, supernatant was collected after 24 h

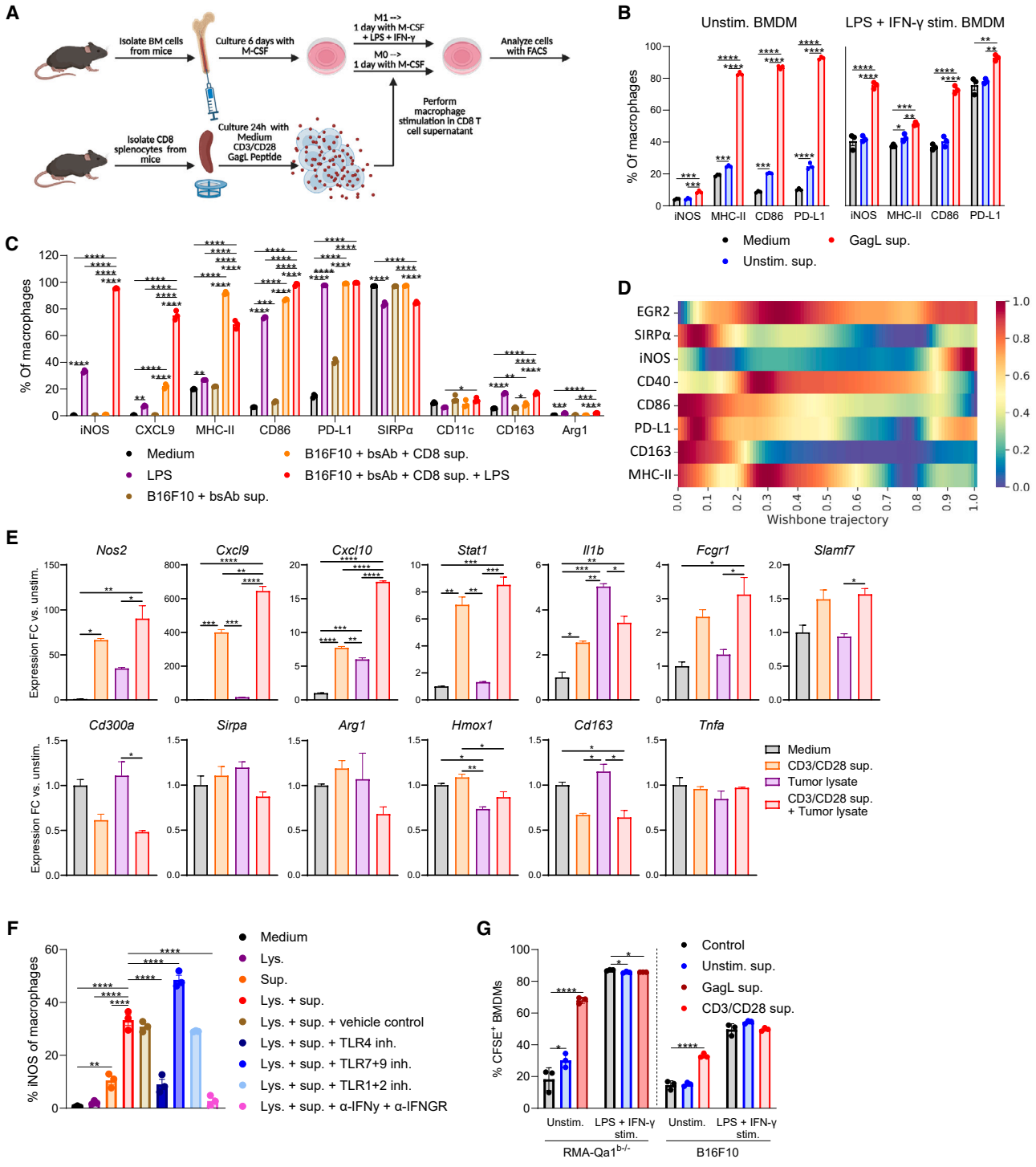

Figure 4. Activated T cells can induce activated functional M1 macrophages

(A) Experimental setup for the generation of BMDMs stimulated with supernatant of $CD8^+$ T cells and/or LPS + IFN-γ. Expression of phenotypic markers on BMDMs after stimulation with supernatant from (B) splenic $CD8^+$ T cells or from (C) intratumoral $CD8^+$ T cells that were pre-incubated with B16F10 tumor cells and bsAb.

(D) Wishbone trajectory analysis of phenotypic markers on tumor macrophages from RMA-$Qa1^{b-/-}$ tumors.

(E) Relative gene expression as determined by qRT-PCR of BMDMs. Tumor lysate is derived from B16F10 tumors.

(F) Expression of iNOS on cultured BMDMs, using supernatant from activated $CD8^+$ T cells and tumor lysate from a mixture of B16F10 and RMA-$Qa1^{b-/-}$ tumor cell lines in the presence of TLR inhibitors and IFN-γ(R) blockade.

(legend continued on next page)

and used to stimulate the BMDMs. Again, a strong M1-like macrophage polarization, indicated by increased expression of iNOS, CXCL9, MHCII, and CD86, was observed (Figure 4C), corroborating the results obtained using splenic CD8$^+$ T cells (Figure S5B). Utilization of Wanderlust analysis on macrophages isolated directly from tumors of vaccinated animals showed that while the vaccine-induced installation of M1-like macrophages occurs early on (represented by an early expression of CD40, CD86, and MHCII), the induction of iNOS occurred later (Figure 4D). This suggests that iNOS expression represents a late-stage activated phenotype of M1-like macrophages.

Although stimulation of BMDMs with T cell supernatant resulted in the induction of iNOS, the fraction of iNOS$^+$ macrophages did not resemble the frequencies we observed *in vivo* (Figures 2I and 2J) or after M1 stimulation involving the TLR ligand LPS (Figures 4B and 4C). We therefore interrogated the presence of endogenous Toll-like receptor (TLR) ligands in the tumor that could aid CD8$^+$ T cells with the polarization of incoming monocytes/macrophages towards their late-stage activated iNOS$^+$ M1-like state. Scrutiny of the transcriptomic datasets revealed the presence of multiple TLR2 and 4 agonists, including HMGB1 and several S100a proteins[23,24](Figures S5C and S5D). Therefore, unstimulated BMDMs were treated with whole tumor lysate in combination with supernatant from activated CD8$^+$ T cells. While stimulation with T cell supernatant or whole tumor lysate alone could induce the gene expression of pro-inflammatory markers associated with an M1-like late-stage macrophage signature (e.g., *Nos2*, *Cxcl9*, *Cxcl10*, *Stat1*), combined stimulation further enhanced their activation (Figures 4E and S5E). In contrast, the expression of genes associated with an anti-inflammatory M2-like signature (*Hmox1*, *Cd163*) was decreased. These findings were confirmed on protein level by flow cytometry, where the addition of whole tumor lysate doubled the population of iNOS$^+$ macrophages, to a percentage similar to that observed *in vivo* following our two immunotherapies (Figure S5F). Furthermore, we confirmed the expression of M1-like markers *Nos2*, *Cxcl9*, and *Cxcl10* in macrophages isolated from treated B16 tumors (Figure S5G). Finally, to determine which factors in the tumor lysate and T cell supernatant contributed to the M1-like macrophage phenotype, we stimulated BMDMs with tumor cell lysate and/or supernatant from activated CD8$^+$ T cells in the presence of different TLR signaling inhibitors and examined the expression of the late-stage M1-like marker iNOS. Inhibition of TLR4 signaling, but not TLR1+2 or TLR7+9, prevented the increase in iNOS$^+$ cells mediated by tumor lysate. Simultaneous blockade of IFN-γ and the IFN-γR also prevented iNOS expression. This demonstrates that TLR4 ligands and IFN-γ in the TME are both essential for M1-like macrophage differentiation (Figure 4F).

M1-like macrophages can utilize several anti-tumor effector functions in the TME,[25,26] including phagocytosis or cytokine-mediated cell death. We therefore interrogated if the effector functions of unstimulated BMDMs were enhanced upon stimulation with activated T cell supernatant and tumor lysate. Indeed, culturing unstimulated macrophages with supernatant from activated T cells and/or tumor lysate showed that both increased phagocytosis of tumor cells (Figures 4G and S5H). The strongest increase was observed with activated T cell supernatant, indicating that CD8$^+$ T cell-derived soluble factors can activate the tumoricidal function of M1-like macrophages. These findings were corroborated by downregulated expression of the phagocytosis inhibitory receptor *Cd300a* and increased expression of *Slamf7* and *Fcgr1*, both encoding phagocytosis-promoting "eat-me" receptors[27–29] (Figures 4E and S5E). Alternatively, the induction of *Tnfa* was only observed when BMDMs were stimulated with RMA-Qa1$^{b-/-}$ tumor lysate and T cell supernatant (Figures 4E and S5E), but no difference in tumor cell death was observed in the presence of a TNF-α inhibitor (Figure S5I). Based on this, we speculate that killing of RMA-Qa1$^{b-/-}$ and B16 tumor cells by macrophages is mostly dominated by phagocytosis and not cytokine-mediated cell death. Importantly, these data suggest that within the context of the TME, CD8$^+$ T cells can install a tumor-phagocytic M1-like macrophage population.

Late-stage activation of macrophages depends on the CCR5-mediated co-localization with CD8$^+$ T cells

Next, we set out to determine what soluble factors were produced by CD8$^+$ T cells that drive the installation of M1-like macrophages. To do so, we re-examined two sets of transcriptomic data, one from the responders/non-responders from the RMA-Qa1$^{b-/-}$ model and another from our combined vaccination and CD3 bsAb approach,[20] for increased expression of chemokines and cytokines in pathways known to attract and activate macrophages.[30–36] Three of such pathways were enriched in both tumor models: (i) CCL3, CCL4, CCL5, and their receptor CCR5, (ii) expression of LTB, and (iii) expression of IFN-γ (Figure 5A). In addition, increased expression of LTBR and type 1 interferons was detected in the RMA-Qa1$^{b-/-}$ model. We confirmed the production and secretion of CCL3, CCL4, CCL5, and IFN-γ by CD8$^+$ T cells on a protein level by isolating CD8$^+$ T cells from spleens or tumors of B16-bearing mice treated with vaccine + bsAb and subsequentially stimulated them with CD3/CD28 beads (Figure 5B).

The effect of IFN-γ signaling, a known polarizer of macrophages towards a pro-inflammatory phenotype,[36,37] resulted in the expression of MHCII, CD86, and PD-L1 in a high percentage of cells (Figure S6A). To promote expression of iNOS in the majority of BMDMs, however, TLR4-mediated signaling was required (Figures 4F and S6A). Previously, CCR5 signaling was suggested to promote iNOS expression,[33,38] but no decrease in iNOS expression was observed in the presence of the CCR5 inhibitor maraviroc[39] (Figure S6B), indicating that CCR5 signaling does not have a direct effect on iNOS expression.

The main function of the CCR5 or LTBR pathways is to respond to their cognate cytokines involved in the direct or indirect attraction of immune cells. Analysis of the TME following CCR5 blockade revealed a decrease in iNOS expression by macrophages in the TME of RMA-Qa1$^{b-/-}$ tumors, to the level

(G) Phagocytosis of IgG-opsonized irradiated tumor cells by BMDMs following indicated BMDM stimulations. Unstim., unstimulated; sup., supernatant; lys., tumor lysate; inh., inhibitor. Data represented as mean ± SEM (B and C, E–G) or mean (D) for $n = 3$ (B–D, F, and G) or $n = 2$ (E). Significance was calculated using one-way ANOVA and Tukey's post hoc tests comparing all groups (B and C, E–G). Significance is only shown for relevant comparisons (C, F, and G). Statistical significance is shown as * = $p < 0.05$, ** = $p < 0.01$, *** = $p < 0.001$, and **** = $p < 0.0001$. See also Figure S5.

A

	Resp. vs. Unt.			Vacc. + bsAb vs. Unt.		
	FC	p-adj.	Rank	FC	p-adj.	Rank
CCL3	3.364	0.040	130	19.29	5.55E-07	111
CCL4	5.134	0.031	36	73.52	1.96E-07	68
CCL5	7.890	0.028	28	210.84	5.82E-09	14
CCR5	2.585	0.047	178	8.82	1.62E-06	146
LTB	3.434	0.018	2	15.35	6.17E-08	41
LTBR	2.178	0.022	71	0.99	0.942	586
IFNa1	3.095	0.051	194	N/A	N/A	N/A
IFNb1	2.868	0.148	399	N/A	N/A	N/A
IFNg	2.621	0.076	276	64.45	3.25E-06	159

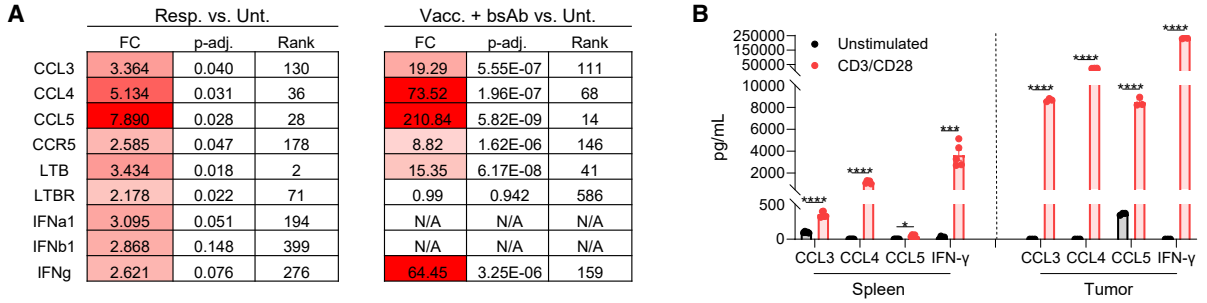

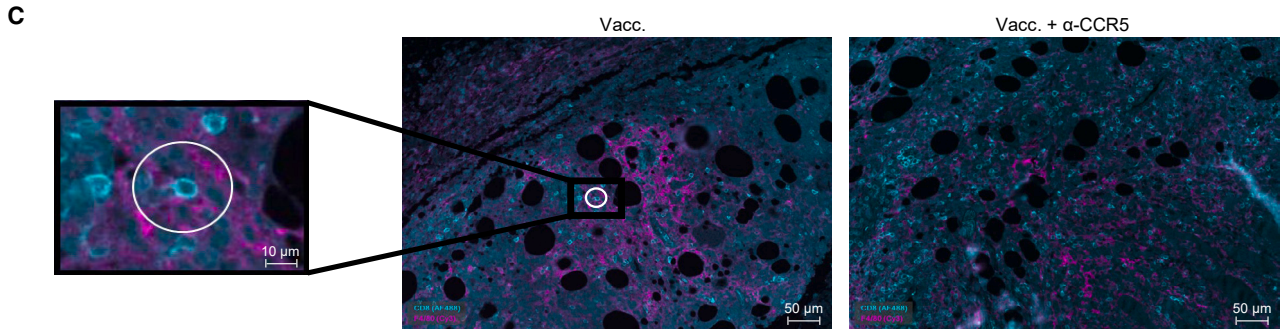

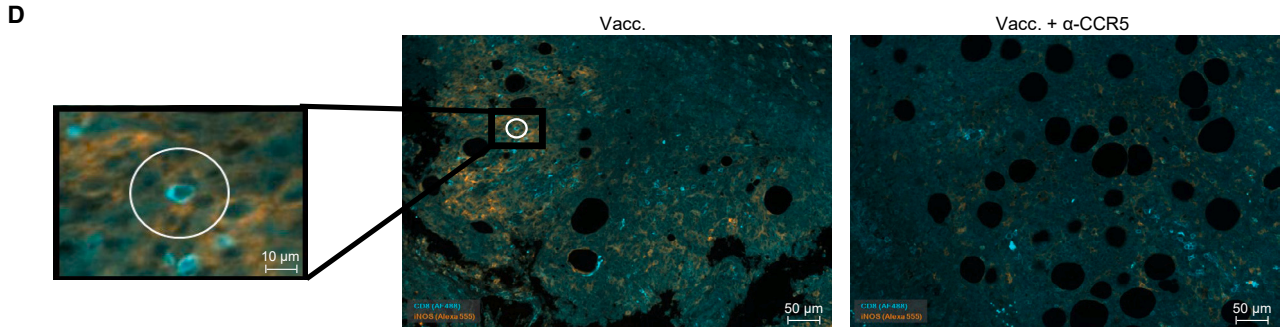

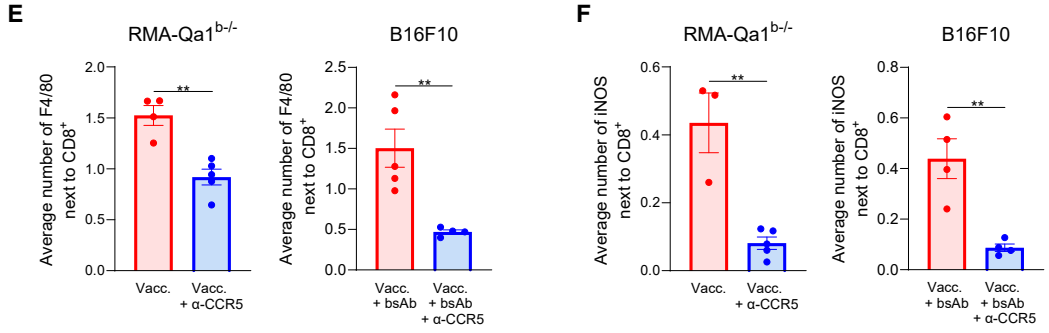

Figure 5. CCR5 signaling is required for intratumoral CD8-M1 macrophage clusters

(A) Selection of DEGs in RMA-Qa1$^{b-/-}$ (left) or KPC3-TRP1 (right) tumors from transcriptomic analysis using nSolver software. Resp, responder; unt., untreated; vacc., vaccination.

(B) Production of CCL3, 4, and 5 and IFN-γ by CD8$^+$ T cells isolated from pooled spleens or B16F10 tumors from vacc. + bsAb-treated mice. Dual immunofluorescence staining of (C) CD8 (cyan) and F4/80 (purple) cells or (D) CD8 (cyan) and iNOS (orange) and colocalization analysis of (E) F4/80 or (F) iNOS next to a CD8$^+$ cell for ~1,000 counted CD8$^+$ cells per treatment group in RMA-Qa1$^{b-/-}$ or ~800 CD8$^+$ T cells in B16F10 tumors. Data represented as mean (A), or mean ± SEM (B, E, and F) for $n = 3–5$ (A) or $n = 3–5$ (B, E, and F). Scale bars represent 10 or 50 μm. Significance was calculated using unpaired two-sided t tests (A, B, E, and F) with Benjamini-Hochberg correction for multiple comparisons (B). Statistical significance is shown as * = $p < 0.05$, ** = $p < 0.01$, *** = $p < 0.001$, and **** = $p < 0.0001$. See also Figures S6 and S7.

of expression seen in untreated tumors (Figures S6C–S6E). Addition of LTBR blockade did not further enhance this effect. No significant impact of CCR5 blockade on other immune cells, both in number and phenotype, was observed (Figures S6F–S6I). Flow cytometry analysis revealed all iNOS$^+$ macrophages to be positive for CCR5, explaining why specifically this population was affected by CCR5 blockade (Figure S6J). These findings were confirmed in the B16 model, where blockade of CCR5 affected neither the immune cell composition nor the phenotype of effector cells, while it reduced the expression of iNOS on macrophages (Figures S7A–S7E).

As the expression of iNOS relies on CCR5 signaling, we hypothesized that in order to adopt a late-stage activation profile, it is necessary for macrophages to be attracted close to the T cells within the tumor via the production of a CCR5 ligand gradient. To test this, we first validated the dependency of iNOS expression on a high cytokine gradient produced by CD8$^+$ T cells. Indeed, if the percentage of activated T cell supernatant added to the BMDM culture was decreased, a specific reduction in iNOS expression, but not other M1 markers, was found (Figure S7F). These effects were likely driven by IFN-γ in the supernatant as iNOS expression was dependent on the dose of IFN-γ (Figure S7G) or the percentage of supernatant added (Figure S7H). Indeed, blockade of IFN-γ signaling completely abolished the induction of iNOS by tumor lysate and activated T cell supernatant (Figure S7H). These data suggested that proximity to IFN-γ-producing T cells is crucial for macrophage differentiation towards a late-stage M1-like phenotype. To verify this close-range interaction between T cells and macrophages in the TME and its dependency on the CCR5 axis, we performed dual immunofluorescence staining of CD8 and F4/80 to examine the spatial interaction between macrophages and CD8$^+$ T cells in the TME of both tumor models. Quantification of the number of macrophages in close proximity to a total of ∼1,000 counted CD8$^+$ T cells (Figure S7I) revealed a significant reduction in macrophage-CD8 clusters following CCR5 blockade in both RMA-Qa1$^{b-/-}$ and B16 tumors (Figures 5C and 5E). In addition, dual staining of iNOS and CD8 showed that this reduction in macrophage-CD8 T cell clusters coincided with a decrease in the number of iNOS$^+$ cells in close proximity to an intratumoral CD8$^+$ T cell (Figures 5D and 5F), corroborating the dependency of iNOS expression on the CCR5-chemokine gradient. Together, these results show that CD8-macrophage cluster formation depends on the CCR5 axis, allowing macrophages to be exposed to optimal concentrations of T cell-produced IFN-γ, required for the induction of iNOS expression.

Late-stage activated M1-like macrophages can deprive lymphomas of L-arginine

Since iNOS-mediated release of the radical nitric oxide (NO) can directly induce immunogenic tumor cell death,[40,41] we investigated if iNOS itself contributed to tumor control. For this purpose, we inoculated wild-type (WT) or iNOS knockout animals (iNOS$^{-/-}$) with RMA-Qa1$^{b-/-}$ or B16 tumors and monitored responses to the different immunotherapies. For RMA-Qa1$^{b-/-}$, the therapeutic effect of the vaccination was completely ablated in iNOS$^{-/-}$ animals, as none of the mice survived (Figure 6A). Moreover, only 10% of the iNOS$^{-/-}$ mice displayed tumor regression following therapy, in contrast to 83% for the WT animals (Figure 6B). In the B16 model, the iNOS gene did not play a role in tumor control (Figure 6C). To exclude that the clinical effect of iNOS knockout was due to intrinsic differences between the mice, we compared the TMEs of vaccinated RMA-Qa1$^{b-/-}$ tumors from WT and iNOS$^{-/-}$ animals. The lack of response to vaccination in iNOS$^{-/-}$ animals could neither be attributed to reduced immune cell infiltration (Figures 6D and S8A), nor differences in the spatial location (Figures S8B and S8C) or reduced effector function (Figure 6E) of intratumoral CD8$^+$ T cells. Rather, their effector phenotype appeared to be enhanced in iNOS$^{-/-}$ tumors, based on increased expression of CD44, CD49a, and Tbet and the increased production of granzyme B. Furthermore, no major effect of iNOS deficiency was seen with respect to the phenotype of macrophages and neutrophils (Figures 6F and S8D). Together, these findings strongly imply a direct effector function of iNOS in vaccination-mediated tumor regression in the RMA-Qa1$^{b-/-}$ model, but not in the B16F10 model.

The anti-tumor efficacy of iNOS is likely related to its function—conversion of L-arginine into L-citrulline and release of NO—which may kill tumor cells.[26] Quantification of nitrite (formed by spontaneous oxidation of NO) by Griess reaction assay confirmed the release of NO by cultured M1-polarized BMDMs (Figure 6G). However, no clear difference in tumor cell death was observed when tumor cells were co-cultured with BMDMs derived from either WT or iNOS$^{-/-}$ mice, with the exception of a small reduction in RMA-Qa1$^{b-/-}$ kill by M1 BMDMs when derived from iNOS$^{-/-}$ mice (Figure S8E). In addition, when unstimulated and M1 BMDMs from WT animals were co-cultured with RMA-Qa1$^{b-/-}$ tumors cells in the presence of the nitric oxide donor Noc18, this did not increase tumor cell death (Figure S8F), suggesting that NO-mediated tumor cell death was not the major mechanism underlying iNOS-dependent tumor regressions. Furthermore, the phagocytic capacity of macrophages was not hampered by the lack of iNOS (Figure S8G). Altogether, these data indicate that the contribution of iNOS to tumor control is not via phagocytosis or NO-mediated cytotoxicity.

Then, we hypothesized that the iNOS-mediated conversion of L-arginine depleted the tumor cells of a highly necessary nutrient. Therefore, RMA-Qa1$^{b-/-}$ and B16 tumor cells were cultured in the presence of varying concentrations of L-arginine. Indeed, the survival of RMA-Qa1$^{b-/-}$ tumor cells was highly correlated (R^2 = 0.9994) to the levels of available L-arginine in the culture medium, which was not the case for the non-lymphoid B16 tumor cells (R^2 = 0.1162) (Figure 6H). The L-arginine dependency of lymphoma cells explains why RMA-Qa1$^{b-/-}$, but not B16 tumors, are strongly affected by the presence of iNOS. Altogether, these results suggest there may be an additional tumor model-selective effector mechanism used by late-stage activated M1-like macrophages via the iNOS-mediated conversion of the critical nutrient L-arginine.

The presence of late-stage activated M1-like macrophages correlates with the response to immunotherapy in mice and humans

To gain a better understanding of the intratumoral M1-like macrophages, we performed single-cell RNA sequencing

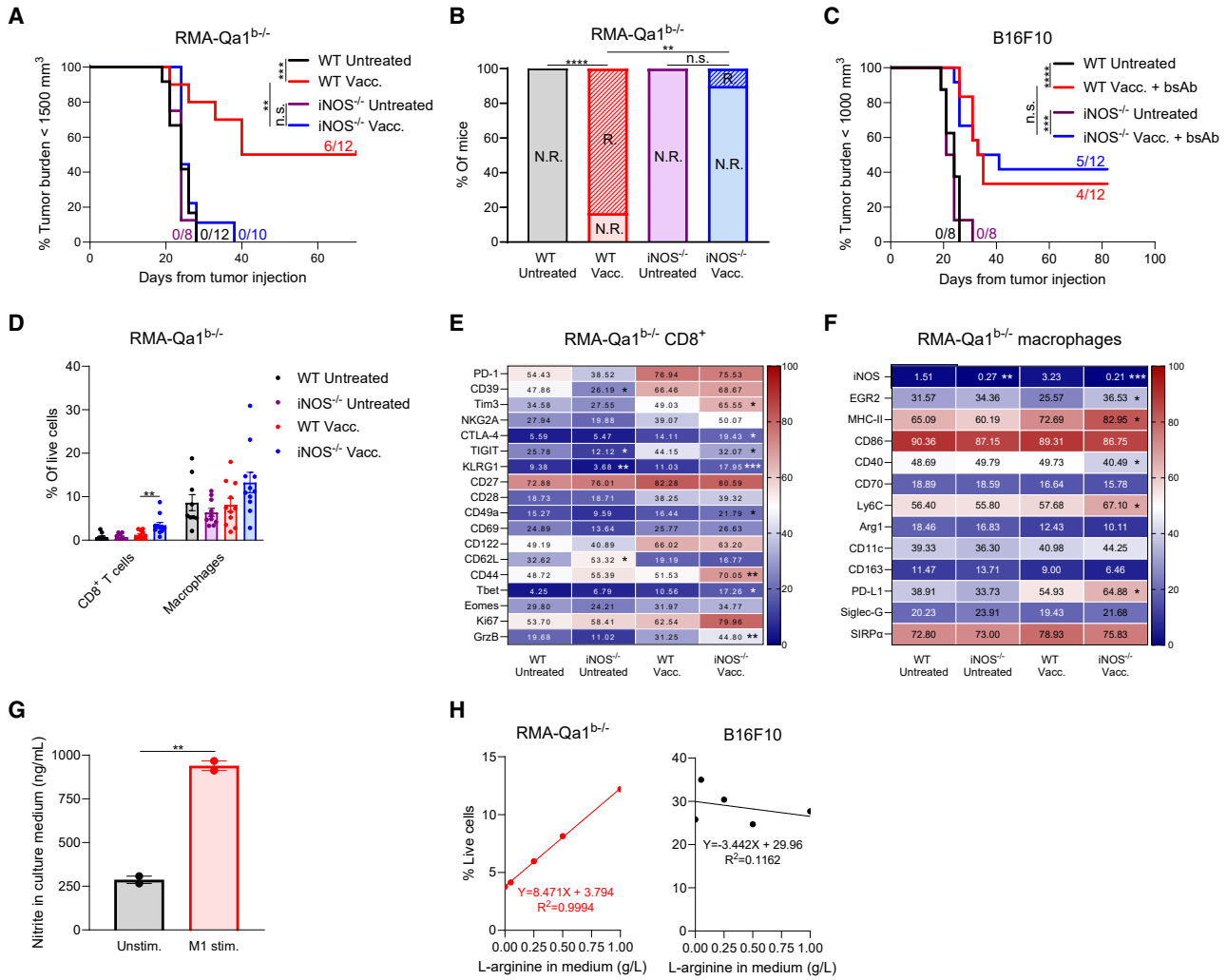

Figure 6. iNOS can act as an effector molecule by depriving tumor cells of L-arginine

(A) Kaplan-Meier graph and (B) treatment responses in mice bearing RMA-Qa1$^{b-/-}$ tumors, treated according to the treatment schedule in Figure 2A. R., responder; N.R., non-responder. (C) Kaplan-Meier survival graphs in mice bearing B16F10 tumors, treated according to the treatment schedule in Figure 2B. Intratumoral frequencies (D) and phenotype of (E) CD8$^+$ T cells and (F) macrophages in mice bearing RMA-Qa1$^{b-/-}$ tumors.

(G) Quantification of nitrite production by cultured BMDMs according to the treatment schedule in Figure 4A.

(H) Dependence of tumor cell viability on the presence of L-arginine in serum-deprived culture medium. Data represented as mean ± SEM (D, G) or mean (E, F) for n = 9–11 (D–F) or n = 2 (G). Significance was calculated using Mantel-Cox log rank tests (A, C), Fisher's exact tests (B), or unpaired two-sided t tests (D–G) comparing WT and iNOS$^{-/-}$ for each treatment (D–F). Statistical significance is shown as * = $p < 0.05$, ** = $p < 0.01$, *** = $p < 0.001$, and **** = $p < 0.0001$. See also Figure S8.

(scRNA-seq) on MHCII$^+$ and MHCII$^-$ macrophage populations (CD11b$^+$F4/80$^+$) isolated from responding RMA-Qa1$^{b-/-}$ tumors. T-SNE embedding based on differential gene expression resulted in the distinction of 10 monocyte and macrophage populations of varying phenotypic states (Figures 7A–7D, and Table S1). Clusters were defined based on their top differentially expressed genes (DEGs), which revealed the anti-inflammatory nature of immune-suppressive C1q+ macrophages (clusters 0 and 1), tissue-resident alternatively activated macrophages (cluster 4), immature macrophages (cluster 5), monocytic myeloid-derived suppressor cells (cluster 7), and angiogenic wound healing macrophages (cluster 9) (Figure 7C, and Table S2). In addition, a pro-inflammatory signature was revealed in IFN-responsive monocytes (cluster 2), late-stage activated M1-like macrophages (cluster 3), and cytokine-producing macrophages (cluster 8), as well as a mixed signature (cluster 6). The expression of *Nos2* (iNOS) was enriched in cluster 3. Pseudotime analysis revealed that cluster 3 was the furthest in the trajectory (Figure 7D), underpinning the late-stage differentiated nature of these macrophages, as deduced earlier by the wishbone trajectory analysis (Figure 4D). Furthermore, gene set enrichment analysis (GSEA) revealed this cluster to be characterized by a pro-inflammatory signature, with increased motility and cell killing capacity (Figure 7E) and with high expression of *Cxcl9*, *Cxcl10*, and the TLR-responsive genes *Sod2* and *Acod1* (Figure 7C, and Table S2).

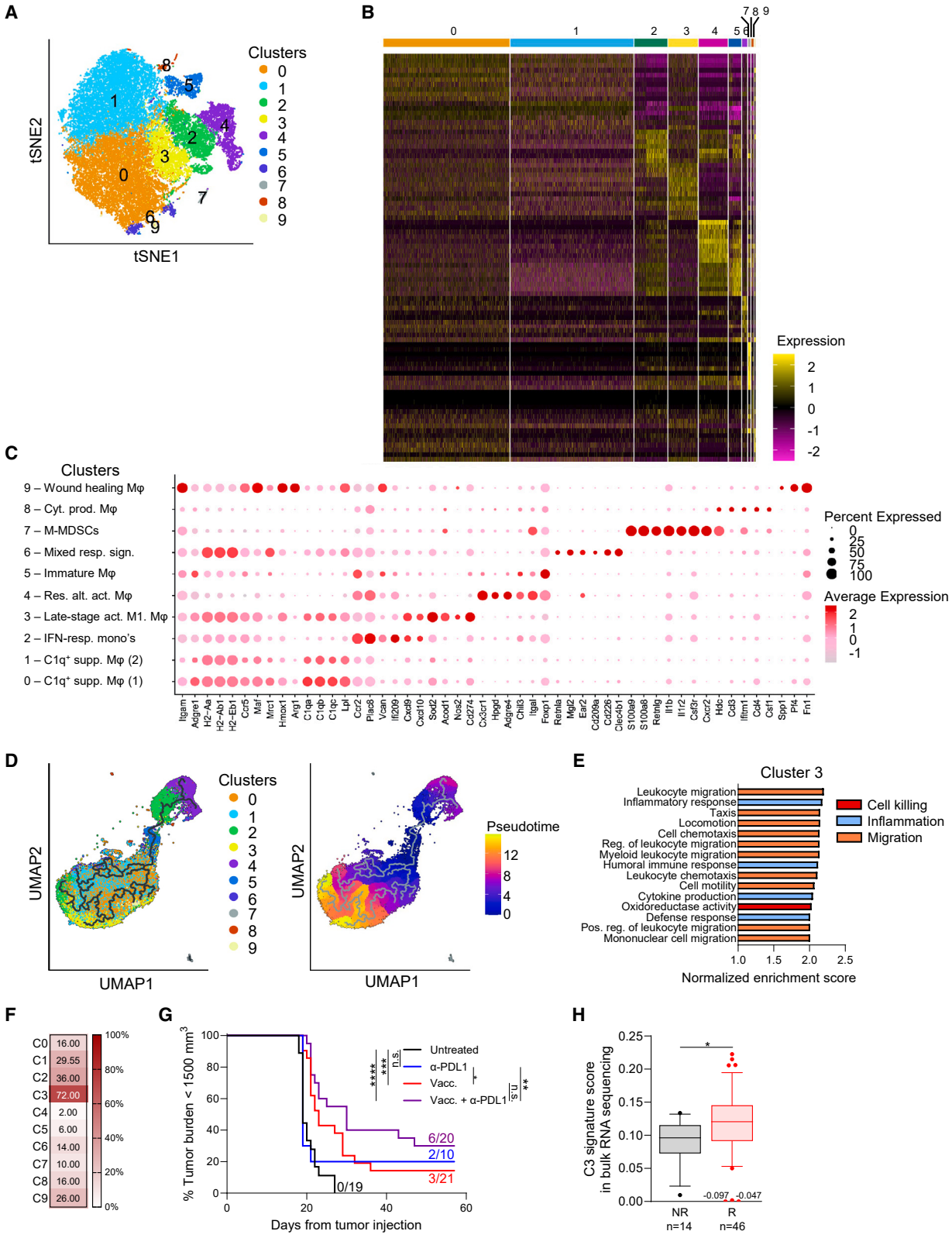

Figure 7. Macrophages in responding tumors exhibit a late-stage activated M1-like phenotype

(A–E) Single-cell RNA sequencing on intratumoral macrophages from RMA-Qa1$^{b-/-}$ tumors. (A) Distribution of the different clusters on t-SNE plots. Phenotype of the different clusters represented as (B) a heatmap showing the top 10 DEGs per cluster and (C) a dot plot showing a selection of DEGs. Mφ, macrophages; Supp.,

(legend continued on next page)

It was previously reported that the presence of a pro-inflammatory macrophage population (called M3) correlated with response to checkpoint inhibitors in the CT26 colon carcinoma tumor model.[42] This tumor model is known to develop an active, but insufficient anti-tumor T cell response. When we compared this macrophage population (M3) to the 10 monocyte/macrophage clusters from our RNA sequencing (RNA-seq) data (C0-9, Figure 7), 72% of the top 50 DEGs from our late-stage activated M1-like macrophage cluster C3 was found to overlap with the DEGs from the M3 macrophages (Figure 7F). Spearman correlation analysis confirmed this overlap, as the M3 cluster only showed significant correlation to the top 50 DEGs from cluster C3, but not other clusters (Figure S8H). As the late-stage activated M1-like macrophages, represented by C3, were highly similar to the ICI responsiveness-associated macrophage population M3, we wondered if the vaccine-induced presence of this macrophage population also sensitized the ICI-resistant tumor model RMA-Qa1$^{b-/-}$ to treatment with checkpoint blockers. Indeed, while α-PD-L1 monotherapy rendered minimal tumor control, it improved the clinical response after therapeutic vaccination (Figure 7G). We then interrogated whether the presence of this macrophage subset in human tumors is associated with a better outcome to ICI treatment, and as such, an active T cell response. To achieve this, we explored the presence of our late-stage activated M1-like macrophage C3 signature in patients that received α-PD-1-based immunotherapies for melanoma (Cohort IRB 15-0837 and 14-0735, University of Chicago). Despite the fact that these macrophages only represent a small percentage of total immune cells in the TME, bulk RNA-seq of tumor biopsies revealed an enrichment in the gene signature of late-stage activated M1-like macrophages in patients displaying a clinical response to ICI (Figure 7H).

A highly similar single human macrophage population is present in multiple tumors and associated with immune checkpoint inhibition responsiveness

The correlation between a higher murine C3 gene profile score and a better response to ICI in patients indicated the presence of a similar macrophage population in human tumors. To pinpoint this exact population, we compared the murine C3 macrophage signature to human macrophage populations identified by Mulder and colleagues across tissues in health and disease.[43] This revealed a strong overlap between the murine C3 macrophage signature and that of human Mulder macrophage cluster #6 (Figures 8A–8C). Human Mulder macrophage cluster #6 is enriched in several tumor types while being less prevalent in healthy tissue (Figure 8D). Interestingly, this cluster was reported to exhibit a strong M1 and phagocytic program for which IFN-γ was predicted as the top upstream regulator. In addition, there was a good relationship between the presence of IFN-γ$^+$ CD8$^+$ T cells and these macrophages.[43] Moreover, these macrophages were shown to express high levels of MHCII, CD86, and PD-L1 at the protein level, directly validating their similarity to our murine M1-like macrophages.[43] GSEA revealed this cluster to be of pro-inflammatory nature with cell killing capacity (Figure 8E) and is further characterized by high expression of *CXCL9*, *CXCL10*, the TLR-responsive genes *SOD2* and *PSME2*, and phagocytic macrophage markers including *CD38* and *GBP5*.[6,44–47] This cluster is enriched in patients with breast cancer (Figure 8D) for which a scRNA-seq dataset containing all cells in the TME was available. This dataset comprised pre- and on-treatment biopsies of 40 breast cancer patients treated with neo-adjuvant α-PD-1 (clinical trial NCT03197389),[48] for which T cell clonotype expansion was used as surrogate for treatment response. We analyzed the monocyte/macrophage populations in this patient cohort (Figure 8F) and projected the gene signature of human Mulder cluster #6 macrophages over these populations. This revealed a near complete overlap with positive treatment response (Figures 8G and 8H). Furthermore, human Mulder cluster #6 signature was highly enriched in macrophage cluster 0 of the breast cancer cohort (Figure 8I).

As expected, GSEA revealed these breast cancer cluster 0 macrophages to display a pro-inflammatory state and activation of cell killing pathways (Figure 8J). To confirm that human breast cancer cluster 0 indeed represented the late-stage activated M1-like macrophages found in our murine models, we compared the gene signature of murine cluster C3 to the monocyte/macrophage populations from this breast cancer cohort. The expression of the C3 signature in these cell populations was nearly identical to that observed for human Mulder cluster #6 (Figures 8H and 8K), identifying human breast cancer cluster 0 as most similar to murine cluster 3 (Figure 8L). Importantly, breast cluster 0 was specifically enriched in pre- and on-treatment tumor samples of patients that respond to neo-adjuvant α-PD-1 (Figure 8M).

Based on our murine data, the presence of M1-like macrophages in breast cancer patients would predict increased levels of tumor-reactive T cells, expressing CCR5 ligands. This, in turn, would allow us to assess if T cell-derived CCR5 ligands play a role in the attraction of breast cancer cluster 0 macrophages. To address this, we zoomed in on the T cells in the same cohort of breast cancer patients.[48] T-SNE embedding revealed the presence of several CD8$^+$ and CD4$^+$ T cell clusters, in which we highlighted the clusters as defined by Bassez et al.[48] (Figures S9A–S9C) Among these, CD8$^+$_Experienced, CD8$^+$_Experienced_proliferating, CD4$^+$_Experienced, and CD4$^+$_Experienced_proliferating clusters

immunosuppressive; IFN-resp mono's, IFN-responsive monocytes; act., activated; Res. alt. act., tissue-resident alternatively activated; Mixed resp. sign., mixed response signature; M-MDSCs, monocytic myeloid-derived suppressor cells; Cyt. Prod., cytokine-producing. (D) Overlay of identified clusters in UMAP plot (left) and visualization of the ordered trajectory by coloring cells based on pseudotime in UMAP (right). (E) GSEA on the pre-ranked DEGs from macrophage cluster 3 using the gene ontology biological process gene sets from the Broad Institute. Reg., regulation; Pos., positive.

(F) Comparison between macrophage clusters from A–D and a single-cell RNA sequencing macrophage cluster that is upregulated in ICI-responsive mice bearing CT26 tumors, showing the percentage from the overlapping genes in the top 50 hits from our clusters.

(G) Kaplan-Meier graph of mice bearing RMA-Qa1$^{b-/-}$ tumors treated with vaccination and/or α-PD-L1.

(H) Boxplot of median, interquartile range, and 10–90 percentile whiskers representation of our C3 signature in tumors analyzed by bulk RNA sequencing of responding (R) or non-responding (NR) melanoma patients. Significance was calculated using Mantel-Cox log rank tests (G), or unpaired two-sided t tests (H). Statistical significance is shown as * = $p < 0.05$, ** = $p < 0.01$, *** = $p < 0.001$, and **** = $p < 0.0001$. See also Figure S8 and Tables S1, and S2.

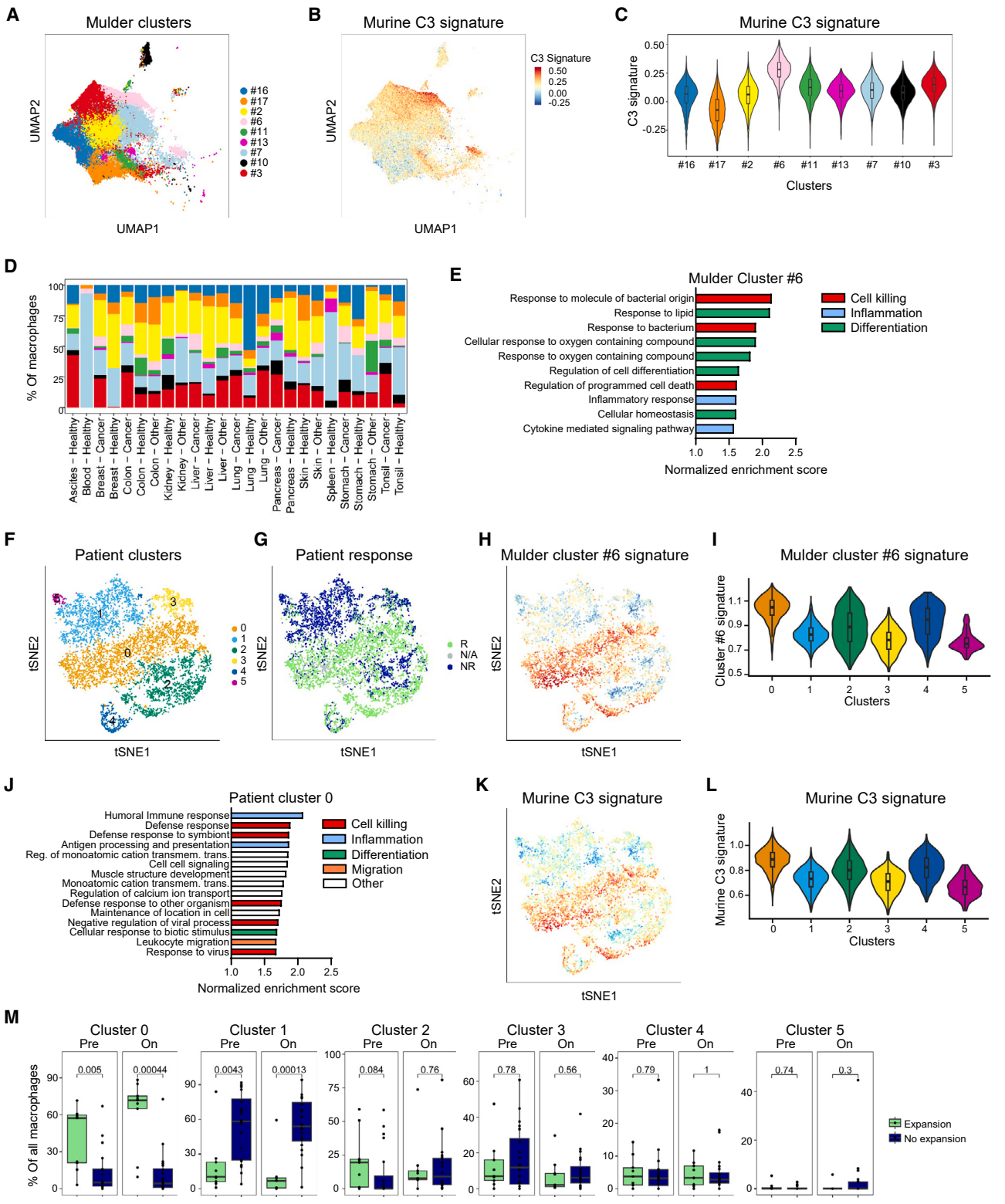

Figure 8. The presence of late-stage activated M1-like macrophages correlates with response to immunotherapy

(A–C) Comparison between single-cell RNA sequencing data containing human macrophage clusters across tissues in health and disease described by Mulder et al. (A) to the murine macrophage C3 signature from Figure 7 displayed on (B) a UMAP or (C) as violin plots.

(D) Distribution of human macrophage clusters identified in A over various tissues.

(legend continued on next page)

delineated tumor-reactive T cells,[48,49] and were enriched in patients that respond to α-PD-1 (Figure S9D). Importantly, these were the only clusters expressing all the three CCR5 ligands, CCL3, CCL4, and CCL5 (Figures S9E, and S9F), similar to intratumoral T cells in our murine models (Figure 5B). Finally, we observed a strong positive correlation between the presence of CCL3/CCL4/CCL5-expressing T cells and breast cancer cluster 0 cells (Figure S9G), sustaining the notion that, similar to mouse, CCR5-ligand producing T cells in human cancers may attract the late-stage activated M1-like macrophages.

To summarize, we have identified a population of late-stage activated M1-like macrophages in human tumors exhibiting an active T cell response using publicly available data. These macrophages are similar to their murine M1-like counterparts and are specifically associated with response to ICI treatment. Furthermore, our analysis identified populations of intratumoral $CD8^+$ and $CD4^+$ T cells in these ICI-responsive patients that express the ligands for CCR5. The presence of these T cell populations positively correlated with the presence of late-stage activated M1-like macrophages. This suggests that the clinical efficacy of T cell-based immunotherapies in human tumors may also hinge on the functional cooperation between $CD8^+$ T cells and late-stage activated M1-like macrophages.

DISCUSSION

In this study, we showed that the response to T cell-based immunotherapy in two different models critically depends on the presence of both T cells and M1-like macrophages. Moreover, we revealed that $CD8^+$ T cells recruit macrophages into the tumor's center of action and attract them to their close vicinity via the CCR5 axis in order to enable their late $iNOS^+$ stage differentiation. In addition to their tumor-phagocytic capacity, these M1-like macrophages expressed the CXCR3 ligands *Cxcl9* and *Cxcl10* that may function as a positive feedback loop for T cell infiltration.[50] Notably, CCL4, CCL5, CXCL9, and CXCL10 have all been associated with the response to T cell-based immunotherapies and improved overall survival in patients.[42,51,52] Finally, we confirmed the presence of these late-stage activated M1-like macrophages in murine and human tumors with activated T cells and revealed an association between their presence and response to ICI.

Co-infiltration of lymphoid and myeloid effector cells, in particular increased infiltration with $CD8^+$ T cells,[53] NK cells,[54] macrophages,[55] and neutrophils,[56] has been described to correlate with the response to immunotherapies and suggests that the intratumoral interaction between these cells is an additional requirement for immunotherapy-induced tumor control.[36,57–59] This notion is corroborated by the observations that a lack of co-operation between lymphocytes and myeloid cells may constitute a resistance mechanism in several murine and human tumors.[1,2,9,14,57,59–61]

The full activation of macrophages in the TME requires the additional signal of endogenous TLR ligands, which are released in the TME upon tumor cell death,[23,24] on top of $CD8^+$ T cell-derived pro-inflammatory cytokines. Interestingly, this coincided with high PD-L1 expression, which is a direct reflection of IFN-γ signaling in tumors with an active immune response.[62] Treatment of RMA-Qa1$^{b-/-}$ tumors in combination with anti-PD-L1 improved clinical outcome that may be explained by enhanced T cell co-stimulation or blockade of previously described reverse signaling of PD-L1.[63] Previous studies have described that $CD4^+$ T cells can contribute to tumor control via IFN-γ-mediated skewing towards more intratumoral $iNOS^+$ M1-like macrophages.[36,64–66] As we find a complete lack in therapeutic response in the absence of iNOS for RMA-Qa1$^{b-/-}$ tumors and a remarkable reduction in survival in both tumor models when only ~50% of total macrophages is depleted, it is possible that the main contribution to tumor control of immunotherapy-activated $CD8^+$ T cells is to kick-start M1-like macrophages. The findings of our study reveal that immunotherapy-driven activation of $CD8^+$ T cells and their cytotoxic mechanisms result in the release of the macrophage-attracting CCR5 ligands, IFN-γ, and tumor-derived TLR4 ligands within the TME. Following this first hit by $CD8^+$ T cells, macrophages infiltrate the tumor, become fully activated, and are a key contributor to tumor control. This is corroborated by the finding that abolishment of IFN-γ production, but not the lytic potential of $CD8^+$ T cells, hampers tumor control.[67] In addition, the 4-fold reduction of intratumoral $CD8^+$ T cells in $CXCR3^{-/-}$ mice bearing TC-1 tumors did not hamper therapy efficacy, while a depletion of effector myeloid cells did.[59] In line with the results of us and others,[56,68,69] this implies that other effector cells may dominate in controlling tumor cell growth at a later stage.

When the anti-tumor effector functions of myeloid cells are studied, the focus often lies on their $CD8^+$ T cell-supportive functions, such as their capacity to attract T cells.[50] However, effector myeloid cells can employ other mechanisms via which they can directly contribute to the anti-tumor immune response. Both macrophages and neutrophils can engage in programmed cell removal[70] of viable tumor cells through phagocytosis (macrophages[71]) or trogocytosis (neutrophils[72]), via which they contribute to tumor control. Unsurprisingly, attempts to unleash the phagocytic potential of effector myeloid cells by blockade of "don't eat me" molecules have thus far been met with promising

(E) GSEA on the pre-ranked DEGs from human macrophage cluster #6 described by Mulder et al. using the gene ontology biological process gene sets from the Broad Institute.
(F) Single-cell RNA sequencing analysis of monocytes/macrophages from pre- and on-treatment tumor biopsies of a human breast cancer cohort, treated with immune checkpoint therapy and (G) their association with treatment response.
(H and I) Similarity of cluster #6 from Mulder et al. to the human breast cancer cohort displayed on (H) tSNE or (I) violin plots.
(J) GSEA on the pre-ranked DEGs from human macrophage cluster 0 of the breast cancer cohort using the gene ontology biological process gene sets from the Broad Institute, Reg., regulation; transmem., transmembrane; trans., transport.
(K and L) Similarity of our C3 signature from murine macrophages to the human breast cancer cohort displayed on (K) tSNE or (L) violin plots.
(M) Boxplots showing the cluster frequencies separated into responding and non-responding tumors, as indicated by T cell expansion for pre- and on-treatment tumor biopsies. Data are represented as boxplots with median, interquartile range and 1.5× interquartile range for pre- and on-treatment biopsies from responders $n = 9$ and non-responders $n = 20$ (M). Significance was calculated using unpaired Mann-Whitney *U*-tests (M). See also Figure S9.

(pre)clinical results.[73–75] Another, more debated, effector mechanism of inflammatory myeloid cells is the iNOS-mediated release of NO. Here, we demonstrate that iNOS is a highly specific marker for late-stage activated M1-like macrophages and that iNOS expression is dependent on stimulation by $CD8^+$ T cell-derived IFN-γ and TLR4 ligands in the tumor cell lysate. Notably, a lack of iNOS does not hamper the phagocytic capacity of macrophages, indicating that these two effector pathways are uncoupled. Early on, iNOS was believed to be a marker for tumor-supportive myeloid cells, as iNOS-derived NO was shown to induce apoptosis of lymphocytes *in vitro*[76,77] and low levels of NO can promote angiogenesis.[78] However, sufficient levels of NO can directly induce immunogenic tumor cell death, simultaneously killing tumor cells and attracting other immune cells to the TME,[40,41] although this was not found in our models. Alternatively, we found that the iNOS-mediated metabolism of L-arginine can lead to a deficit of this critical nutrient in the TME, lack of which may affect the viability of tumor cells, shown here for RMA-Qa1$^{b-/-}$. Noteworthy, as neutrophils from TMEs of responding tumors were also shown to be $iNOS^+$, this tumor-specific sensitivity for L-arginine deprivation could explain why in RMA-Qa1$^{b-/-}$ tumors neutrophils also play a role in immunotherapy-induced regressions, while for B16 tumors this is not the case. An appealing possibility is that the depletion of L-arginine in the tumor slows down tumor growth to a level that is better controllable by $CD8^+$ T cells, ultimately enhancing therapeutic efficacy. Importantly, in the absence of iNOS, the influx and activation level of $CD8^+$ T cells was enhanced after therapeutic vaccination; however, this did not coincide with increased tumor control, stressing the critical role of effector myeloid cells in tumor eradication following T cell-based immunotherapies.

Comparing the murine C3 macrophage signature to human macrophages across tissues in health and disease showed a strong overlap with human Mulder cluster #6. This cluster is enriched in several tumor types, displays an IFN-γ-mediated M1 and phagocytic program, and was predicted to have the highest interaction with IFN-γ producing $CD8^+$ T cells in the tumor.[43] To overcome the lack of on-treatment tumor samples from patients with increased intratumoral T cell frequencies after successful therapeutic vaccination, we instead selected a cohort of ICI-treated patients, for which the presence of tumor-specific T cells in the tumor is a well-known requirement for therapy response.[79] Upon comparing human Mulder signature #6 and our murine signature C3 with macrophage profiles in breast cancer biopsies,[48] we discovered a striking overlap with breast cluster 0. The cluster's presence was strongly associated with ICI responsiveness and increased numbers of experienced $CD8^+$ and $CD4^+$ T cells, able to produce all three ligands for CCR5.

In conclusion, late-stage activated M1-like macrophages are of pivotal importance for the response to T cell-based immunotherapy in murine tumor models and correlated with ICI response in human patients. Earlier studies have reported similar crucial contributions to immunotherapy-mediated tumor control by neutrophils and eosinophils.[56,68,69] The notion that myeloid effector cells are key to the efficacy of T cell-based immunotherapy not only stresses that macrophage or neutrophil-inhibiting therapies (e.g., CSF1R inhibitors,[80] CXCR2 inhibitors[81]) in combination with T cell-based immunotherapies should be used with utmost caution, but also suggests that current efforts to improve T cell-based immunotherapy should focus on the engagement of M1-like macrophages.

Limitations of this study

One limitation of our study concerns the use of therapeutic vaccination as a treatment modality in our murine models while, in analyzed human samples, patients are treated with immune checkpoint inhibition. As our murine models indicate the macrophage phenotype of interest may be present only after immunotherapy-induced $CD8^+$ T cell activation, the analysis of human samples would require on-treatment samples from patients enrolled in a vaccine trial. Unfortunately, scRNA-seq data of on-treatment samples were not available. As the notion that effective checkpoint blockade therapy requires pre-existing tumor-reactive $CD8^+$ T cells is well established and ICI patient datasets are available, we considered such samples to best reflect the situation which we would have obtained after successful vaccination *in vivo*.

A second limitation revolves around the relative contribution of $CD8^+$ T cell and the M1-like macrophages to tumor cell killing. Although out of the scope of the current study, it remains crucial to formally demonstrate how tumor cells are controlled by M1-like macrophages and to what extent T cell-mediated killing mechanisms contribute to tumor regression.

STAR★METHODS

Detailed methods are provided in the online version of this paper and include the following:

- KEY RESOURCES TABLE
- RESOURCE AVAILABILITY
  - Lead contact
  - Materials availability
  - Data and code availability
- EXPERIMENTAL MODEL AND STUDY PARTICIPANT DETAILS
  - Mice
  - Tumor cell lines
- METHOD DETAILS
  - Treatment
  - Flow cytometry
  - Immunohistochemistry
  - Immunofluorescence
  - ELISA
  - Transcriptomics
  - Single cell RNA-sequencing
  - BMDM and co-culture assays
  - Griess reaction
  - L-arginine cell culture
  - Quantitative real-time PCR (qRT-PCR)
  - Quantification and statistical analysis

SUPPLEMENTAL INFORMATION

Supplemental information can be found online at https://doi.org/10.1016/j.ccell.2024.04.011.

ACKNOWLEDGMENTS

This research was funded by the Dutch Cancer Society (KWF) 2021-14339 and Oncode Base Funding to S.H.v.d.B. and a commercial research grant from Genmab to T.v.H. We thank Genmab for providing us with the CD3xTA99 bispecific antibodies. We thank our colleague Ziena Abdulrahman for experimental help. Also, we thank Kristel Kemper for valuable data discussions,

Charlotte Berendsen and Renoud Marijnissen for project management, and Lars Hallander Hansen for intellectual property support. Furthermore, we thank our colleagues from the animal facility, peptide facility, and flow cytometry facility in the LUMC. Finally, graphics of experimental setups were created with BioRender.com.

AUTHOR CONTRIBUTIONS

Conceptualization, S.H.v.d.B. and T.v.H.; data curation, S.H.v.d.B.; formal analysis, M.J.v.E., J.M., C.L., J.R., G.S., and R.T.; funding acquisition, S.H.v.d.B., T.v.H., and J.S.; investigation, M.J.v.E., J.M., C.L., G.S., and M.S.; methodology, M.J.v.E., J.M., T.v.H., and S.H.v.d.B.; project administration, S.H.v.d.B.; software, J.R. and R.T.; supervision, S.H.v.d.B., T.v.H., N.F.C.C.d.M., V.O., K.L., J.S., S.J.R., and T.F.G.; validation, M.J.v.E., J.M., C.L., G.S., and M.S.; visualization, M.J.v.E., J.M., J.R., and R.T.; writing – original draft, M.J.v.E., J.M., and S.H.v.d.B.; writing – review and editing, all.

DECLARATION OF INTERESTS

V.O., K.L., and J.S. are (former) employees of Genmab and have ownership interests (including stock, patents, warrants, etc.). J.M., V.O., K.L., J.S., and T.v.H. are inventors on a patent (WO2022049220A2) involving the combination of CD3 bsAb therapy in combination with vaccination.

Received: September 29, 2023
Revised: February 23, 2024
Accepted: April 24, 2024
Published: May 16, 2024

REFERENCES

1. Fridman, W.H., Pagès, F., Sautès-Fridman, C., and Galon, J. (2012). The immune contexture in human tumours: impact on clinical outcome. Nat. Rev. Cancer *12*, 298–306.
2. Bruni, D., Angell, H.K., and Galon, J. (2020). The immune contexture and Immunoscore in cancer prognosis and therapeutic efficacy. Nat. Rev. Cancer *20*, 662–680.
3. Camus, M., Tosolini, M., Mlecnik, B., Pagès, F., Kirilovsky, A., Berger, A., Costes, A., Bindea, G., Charoentong, P., Bruneval, P., et al. (2009). Coordination of intratumoral immune reaction and human colorectal cancer recurrence. Cancer Res. *69*, 2685–2693.
4. Hiam-Galvez, K.J., Allen, B.M., and Spitzer, M.H. (2021). Systemic immunity in cancer. Nat. Rev. Cancer *21*, 345–359.
5. Neophytou, C.M., Pierides, C., Christodoulou, M.-I., Costeas, P., Kyriakou, T.-C., and Papageorgis, P. (2020). The Role of Tumor-Associated Myeloid Cells in Modulating Cancer Therapy. Front. Oncol. *10*, 899.
6. House, I.G., Savas, P., Lai, J., Chen, A.X.Y., Oliver, A.J., Teo, Z.L., Todd, K.L., Henderson, M.A., Giuffrida, L., Petley, E.V., et al. (2020). Macrophage-Derived CXCL9 and CXCL10 Are Required for Antitumor Immune Responses Following Immune Checkpoint Blockade. Clin. Cancer Res. *26*, 487–504.
7. Broz, M.L., Binnewies, M., Boldajipour, B., Nelson, A.E., Pollack, J.L., Erle, D.J., Barczak, A., Rosenblum, M.D., Daud, A., Barber, D.L., et al. (2014). Dissecting the Tumor Myeloid Compartment Reveals Rare Activating Antigen-Presenting Cells Critical for T Cell Immunity. Cancer Cell *26*, 638–652.
8. Spranger, S., Dai, D., Horton, B., and Gajewski, T.F. (2017). Tumor-Residing Batf3 Dendritic Cells Are Required for Effector T Cell Trafficking and Adoptive T Cell Therapy. Cancer Cell *31*, 711–723.e4.
9. Beyranvand Nejad, E., Labrie, C., Abdulrahman, Z., Van Elsas, M.J., Rademaker, E., Kleinovink, J.W., Van Der Sluis, T.C., Van Duikeren, S., Teunisse, A.F.A.S., Jochemsen, A.G., et al. (2020). Lack of myeloid cell infiltration as an acquired resistance strategy to immunotherapy. J. Immunother. Cancer *8*, e001326.
10. Beatty, G.L., Chiorean, E.G., Fishman, M.P., Saboury, B., Teitelbaum, U.R., Sun, W., Huhn, R.D., Song, W., Li, D., Sharp, L.L., et al. (2011). CD40 agonists alter tumor stroma and show efficacy against pancreatic carcinoma in mice and humans. Science *331*, 1612–1616.
11. Hicks, A.M., Riedlinger, G., Willingham, M.C., Alexander-Miller, M.A., Von Kap-Herr, C., Pettenati, M.J., Sanders, A.M., Weir, H.M., Du, W., Kim, J., et al. (2006). Transferable anticancer innate immunity in spontaneous regression/complete resistance mice. Proc. Natl. Acad. Sci. USA *103*, 7753–7758.
12. Klug, F., Prakash, H., Huber, P.E., Seibel, T., Bender, N., Halama, N., Pfirschke, C., Voss, R.H., Timke, C., Umansky, L., et al. (2013). Low-Dose Irradiation Programs Macrophage Differentiation to an iNOS+/M1 Phenotype that Orchestrates Effective T Cell Immunotherapy. Cancer Cell *24*, 589–602.
13. Chen, J., Ye, X., Pitmon, E., Lu, M., Wan, J., Jellison, E.R., Adler, A.J., Vella, A.T., and Wang, K. (2019). IL-17 inhibits CXCL9/10-mediated recruitment of CD8+ cytotoxic T cells and regulatory T cells to colorectal tumors. J. Immunother. Cancer *7*, 324.
14. Vermare, A., Guérin, M.V., Peranzoni, E., and Bercovici, N. (2022). Dynamic CD8+ T Cell Cooperation with Macrophages and Monocytes for Successful Cancer Immunotherapy. Cancers *14*, 3546.
15. Chmielewski, M., Kopecky, C., Hombach, A.A., and Abken, H. (2011). IL-12 Release by Engineered T Cells Expressing Chimeric Antigen Receptors Can Effectively Muster an Antigen-Independent Macrophage Response on Tumor Cells That Have Shut Down Tumor Antigen Expression. Cancer Res. *71*, 5697–5706.
16. Wang, E., Worschech, A., and Marincola, F.M. (2008). The immunologic constant of rejection. Trends Immunol. *29*, 256–262.
17. van Montfoort, N., Borst, L., Korrer, M.J., Sluijter, M., Marijt, K.A., Santegoets, S.J., van Ham, V.J., Ehsan, I., Charoentong, P., André, P., et al. (2018). NKG2A Blockade Potentiates CD8 T Cell Immunity Induced by Cancer Vaccines. Cell *175*, 1744–1755.e15.
18. Ossendorp, F., Mengedé, E., Camps, M., Filius, R., and Melief, C.J. (1998). Specific T Helper Cell Requirement for Optimal Induction of Cytotoxic T Lymphocytes against Major Histocompatibility Complex Class II Negative Tumors. J. Exp. Med. *187*, 693–702.
19. Jablonski, K.A., Amici, S.A., Webb, L.M., Ruiz-Rosado, J.D.D., Popovich, P.G., Partida-Sanchez, S., and Guerau-De-arellano, M. (2015). Novel Markers to Delineate Murine M1 and M2 Macrophages. PLoS One *10*, e0145342.
20. Middelburg, J., Sluijter, M., Schaap, G., Göynük, B., Lloyd, K., Ovcinnikovs, V., Zom, G.G., Marijnissen, R.J., Groeneveldt, C., Griffioen, L., et al. (2024). T-cell stimulating vaccines empower CD3 bispecific antibody therapy in solid tumors. Nat. Commun. *15*, 48.
21. Benonisson, H., Altıntaş, I., Sluijter, M., Verploegen, S., Labrijn, A.F., Schuurhuis, D.H., Houtkamp, M.A., Verbeek, J.S., Schuurman, J., and van Hall, T. (2019). CD3-Bispecific Antibody Therapy Turns Solid Tumors into Inflammatory Sites but Does Not Install Protective Memory. Mol. Cancer Ther. *18*, 312–322.
22. Sun, J.C., Beilke, J.N., and Lanier, L.L. (2009). Adaptive immune features of natural killer cells. Nature *457*, 557–561.
23. Yu, L., Wang, L., and Chen, S. (2010). Endogenous toll-like receptor ligands and their biological significance. J. Cell Mol. Med. *14*, 2592–2603.
24. Yu, L., Wang, L., and Chen, S. (2012). Exogenous or endogenous Toll-like receptor ligands: which is the MVP in tumorigenesis? Cell. Mol. Life Sci. *69*, 935–949.
25. Mantovani, A., Allavena, P., Marchesi, F., and Garlanda, C. (2022). Macrophages as tools and targets in cancer therapy. Nat. Rev. Drug Discov. *21*, 799–820.
26. Keller, R., Keist, R., Wechsler, A., Leist, T.P., and Van Der Meide, P.H. (1990). Mechanisms of macrophage-mediated tumor cell killing: A comparative analysis of the roles of reactive nitrogen intermediates and tumor necrosis factor. Int. J. Cancer *46*, 682–686.
27. Simhadri, V.R., Andersen, J.F., Calvo, E., Choi, S.-C., Coligan, J.E., and Borrego, F. (2012). Human CD300a binds to phosphatidylethanolamine

and phosphatidylserine, and modulates the phagocytosis of dead cells. Blood *119*, 2799–2809.

28. Chen, J., Zhong, M.-C., Guo, H., Davidson, D., Mishel, S., Lu, Y., Rhee, I., Pérez-Quintero, L.-A., Zhang, S., Cruz-Munoz, M.-E., et al. (2017). SLAMF7 is critical for phagocytosis of haematopoietic tumour cells via Mac-1 integrin. Nature *544*, 493–497.
29. Hawley, K.L., Cruz, A.R., Benjamin, S.J., La Vake, C.J., Cervantes, J.L., LeDoyt, M., Ramirez, L.G., Mandich, D., Fiel-Gan, M., Caimano, M.J., et al. (2017). IFNγ Enhances CD64-Potentiated Phagocytosis of Treponema pallidum Opsonized with Human Syphilitic Serum by Human Macrophages. Front. Immunol. *8*, 1227.
30. Ehlers, S., Hölscher, C., Scheu, S., Tertilt, C., Hehlgans, T., Suwinski, J., Endres, R., and Pfeffer, K. (2003). The Lymphotoxin β Receptor Is Critically Involved in Controlling Infections with the Intracellular Pathogens *Mycobacterium tuberculosis* and *Listeria monocytogenes*. J. Immunol. *170*, 5210–5218.
31. Grandoch, M., Feldmann, K., Göthert, J.R., Dick, L.S., Homann, S., Klatt, C., Bayer, J.K., Waldheim, J.N., Rabausch, B., Nagy, N., et al. (2015). Deficiency in Lymphotoxin β Receptor Protects From Atherosclerosis in apoE-Deficient Mice. Circ. Res. *116*.
32. Yeh, D.Y.-W., Wu, C.-C., Chin, Y.-P., Lu, C.-J., Wang, Y.-H., and Chen, M.-C. (2015). Mechanisms of human lymphotoxin beta receptor activation on upregulation of CCL5/RANTES production. Int. Immunopharmacol. *28*, 220–229.
33. Li, M., Sun, X., Zhao, J., Xia, L., Li, J., Xu, M., Wang, B., Guo, H., Yu, C., Gao, Y., et al. (2020). CCL5 deficiency promotes liver repair by improving inflammation resolution and liver regeneration through M2 macrophage polarization. Cell. Mol. Immunol. *17*, 753–764.
34. Kersten, K., Hu, K.H., Combes, A.J., Samad, B., Harwin, T., Ray, A., Rao, A.A., Cai, E., Marchuk, K., Artichoker, J., et al. (2022). Spatiotemporal co-dependency between macrophages and exhausted CD8+ T cells in cancer. Cancer Cell *40*, 624–638.e9.
35. Dangaj, D., Bruand, M., Grimm, A.J., Ronet, C., Barras, D., Duttagupta, P.A., Lanitis, E., Duraiswamy, J., Tanyi, J.L., Benencia, F., et al. (2019). Cooperation between Constitutive and Inducible Chemokines Enables T Cell Engraftment and Immune Attack in Solid Tumors. Cancer Cell *35*, 885–900.e10.
36. Bogen, B., Fauskanger, M., Haabeth, O.A., and Tveita, A. (2019). CD4+ T cells indirectly kill tumor cells via induction of cytotoxic macrophages in mouse models. Cancer Immunol. Immunother. *68*, 1865–1873.
37. Duluc, D., Corvaisier, M., Blanchard, S., Catala, L., Descamps, P., Gamelin, E., Ponsoda, S., Delneste, Y., Hebbar, M., and Jeannin, P. (2009). Interferon-γ reverses the immunosuppressive and protumoral properties and prevents the generation of human tumor-associated macrophages. Int. J. Cancer *125*, 367–373.
38. Villalta, F., Zhang, Y., Bibb, K.E., Kappes, J.C., and Lima, M.F. (1998). The Cysteine-Cysteine Family of Chemokines RANTES, MIP-1α, and MIP-1β Induce Trypanocidal Activity in Human Macrophages via Nitric Oxide. Infect. Immun. *66*, 4690–4695.
39. Dorr, P., Westby, M., Dobbs, S., Griffin, P., Irvine, B., Macartney, M., Mori, J., Rickett, G., Smith-Burchnell, C., Napier, C., et al. (2005). Maraviroc (UK-427,857), a Potent, Orally Bioavailable, and Selective Small-Molecule Inhibitor of Chemokine Receptor CCR5 with Broad-Spectrum Anti-Human Immunodeficiency Virus Type 1 Activity. Antimicrob. Agents Chemother. *49*, 4721–4732.
40. Vannini, F., Kashfi, K., and Nath, N. (2015). The dual role of iNOS in cancer. Redox Biol. *6*, 334–343.
41. Jiang, W., Dong, W., Li, M., Guo, Z., Wang, Q., Liu, Y., Bi, Y., Zhou, H., and Wang, Y. (2022). Nitric Oxide Induces Immunogenic Cell Death and Potentiates Cancer Immunotherapy. ACS Nano *16*, 3881–3894.
42. Qu, Y., Wen, J., Thomas, G., Yang, W., Prior, W., He, W., Sundar, P., Wang, X., Potluri, S., and Salek-Ardakani, S. (2020). Baseline Frequency of Inflammatory Cxcl9-Expressing Tumor-Associated Macrophages Predicts Response to Avelumab Treatment. Cell Rep. *32*, 107873.
43. Mulder, K., Patel, A.A., Kong, W.T., Piot, C., Halitzki, E., Dunsmore, G., Khalilnezhad, S., Irac, S.E., Dubuisson, A., Chevrier, M., et al. (2021). Cross-tissue single-cell landscape of human monocytes and macrophages in health and disease. Immunity *54*, 1883–1900.e5.
44. Rakkola, R., Matikainen, S., and Nyman, T.A. (2007). Proteome analysis of human macrophages reveals the upregulation of manganese-containing superoxide dismutase after toll-like receptor activation. Proteomics *7*, 378–384.
45. Orecchioni, M., Ghosheh, Y., Pramod, A.B., and Ley, K. (2019). Macrophage Polarization: Different Gene Signatures in M1(LPS+) vs. Classically and M2(LPS–) vs. Alternatively Activated Macrophages. Front. Immunol. *10*, 1084.
46. Li, W., Li, Y., Jin, X., Liao, Q., Chen, Z., Peng, H., and Zhou, Y. (2022). CD38: A Significant Regulator of Macrophage Function. Front. Oncol. *12*, 775649.
47. Feng, S., Enosi Tuipulotu, D., Pandey, A., Jing, W., Shen, C., Ngo, C., Tessema, M.B., Li, F.-J., Fox, D., Mathur, A., et al. (2022). Pathogen-selective killing by guanylate-binding proteins as a molecular mechanism leading to inflammasome signaling. Nat. Commun. *13*, 4395.
48. Bassez, A., Vos, H., Van Dyck, L., Floris, G., Arijs, I., Desmedt, C., Boeckx, B., Vanden Bempt, M., Nevelsteen, I., Lambein, K., et al. (2021). A single-cell map of intratumoral changes during anti-PD1 treatment of patients with breast cancer. Nat. Med. *27*, 820–832.
49. Duhen, T., Duhen, R., Montler, R., Moses, J., Moudgil, T., de Miranda, N.F., Goodall, C.P., Blair, T.C., Fox, B.A., McDermott, J.E., et al. (2018). Co-expression of CD39 and CD103 identifies tumor-reactive CD8 T cells in human solid tumors. Nat. Commun. *9*, 2724.
50. Tokunaga, R., Zhang, W., Naseem, M., Puccini, A., Berger, M.D., Soni, S., McSkane, M., Baba, H., and Lenz, H.-J. (2018). CXCL9, CXCL10, CXCL11/CXCR3 axis for immune activation – A target for novel cancer therapy. Cancer Treat Rev. *63*, 40–47.
51. Vilgelm, A.E., and Richmond, A. (2019). Chemokines Modulate Immune Surveillance in Tumorigenesis, Metastasis, and Response to Immunotherapy. Front. Immunol. *10*, 333.
52. Han, Y., Guo, Z., Jiang, L., Li, X., Chen, J., Ouyang, L., Li, Y., and Wang, X. (2023). CXCL10 and CCL5 as feasible biomarkers for immunotherapy of homologous recombination deficient ovarian cancer. Am. J. Cancer Res. *13*, 1904–1922.
53. Li, F., Li, C., Cai, X., Xie, Z., Zhou, L., Cheng, B., Zhong, R., Xiong, S., Li, J., Chen, Z., et al. (2021). The association between CD8+ tumor-infiltrating lymphocytes and the clinical outcome of cancer immunotherapy: A systematic review and meta-analysis. EClinicalMedicine *41*, 101134.
54. Coca, S., Perez-Piqueras, J., Martinez, D., Colmenarejo, A., Saez, M.A., Vallejo, C., Martos, J.A., and Moreno, M. (1997). The prognostic significance of intratumoral natural killer cells in patients with colorectal carcinoma. Cancer *79*, 2320–2328.
55. Ardighieri, L., Missale, F., Bugatti, M., Gatta, L.B., Pezzali, I., Monti, M., Gottardi, S., Zanotti, L., Bignotti, E., Ravaggi, A., et al. (2021). Infiltration by CXCL10 Secreting Macrophages Is Associated With Antitumor Immunity and Response to Therapy in Ovarian Cancer Subtypes. Front. Immunol. *12*, 690201.
56. Gungabeesoon, J., Gort-Freitas, N.A., Kiss, M., Bolli, E., Messemaker, M., Siwicki, M., Hicham, M., Bill, R., Koch, P., Cianciaruso, C., et al. (2023). A neutrophil response linked to tumor control in immunotherapy. Cell *186*, 1448–1464.e20.
57. van der Sluis, T.C., Sluijter, M., van Duikeren, S., West, B.L., Melief, C.J.M., Arens, R., van der Burg, S.H., and van Hall, T. (2015). Therapeutic Peptide Vaccine-Induced CD8 T Cells Strongly Modulate Intratumoral Macrophages Required for Tumor Regression. Cancer Immunol. Res. *3*, 1042–1051.
58. Schürch, C.M., Bhate, S.S., Barlow, G.L., Phillips, D.J., Noti, L., Zlobec, I., Chu, P., Black, S., Demeter, J., McIlwain, D.R., et al. (2020). Coordinated Cellular Neighborhoods Orchestrate Antitumoral Immunity at the Colorectal Cancer Invasive Front. Cell *182*, 1341–1359.e19.

59. Thoreau, M., Penny, H.L., Tan, K., Regnier, F., Weiss, J.M., Lee, B., Johannes, L., Dransart, E., Le Bon, A., Abastado, J.-P., et al. (2015). Vaccine-induced tumor regression requires a dynamic cooperation between T cells and myeloid cells at the tumor site. Oncotarget *6*, 27832–27846.

60. Fridman, W.H., Zitvogel, L., Sautès–Fridman, C., and Kroemer, G. (2017). The immune contexture in cancer prognosis and treatment. Nat. Rev. Clin. Oncol. *14*, 717–734.

61. Kazama, A., Bilim, V., Tasaki, M., Anraku, T., Kuroki, H., Shirono, Y., Murata, M., Hiruma, K., and Tomita, Y. (2022). Tumor-infiltrating immune cell status predicts successful response to immune checkpoint inhibitors in renal cell carcinoma. Sci. Rep. *12*. 20386. https://doi.org/10.1038/s41598-022-24437-6.

62. Garcia-Diaz, A., Shin, D.S., Moreno, B.H., Saco, J., Escuin-Ordinas, H., Rodriguez, G.A., Zaretsky, J.M., Sun, L., Hugo, W., Wang, X., et al. (2017). Interferon Receptor Signaling Pathways Regulating PD-L1 and PD-L2 Expression. Cell Rep. *19*, 1189–1201.

63. Hartley, G.P., Chow, L., Ammons, D.T., Wheat, W.H., and Dow, S.W. (2018). Programmed Cell Death Ligand 1 (PD-L1) Signaling Regulates Macrophage Proliferation and Activation. Cancer Immunol. Res. *6*, 1260–1273.

64. Fauskanger, M., Haabeth, O.A.W., Skjeldal, F.M., Bogen, B., and Tveita, A.A. (2018). Tumor Killing by CD4+ T Cells Is Mediated via Induction of Inducible Nitric Oxide Synthase-Dependent Macrophage Cytotoxicity. Front. Immunol. *9*, 1684.

65. Hung, K., Hayashi, R., Lafond-Walker, A., Lowenstein, C., Pardoll, D., and Levitsky, H. (1998). The Central Role of CD4+ T Cells in the Antitumor Immune Response. J. Exp. Med. *188*, 2357–2368.

66. Kruse, B., Buzzai, A.C., Shridhar, N., Braun, A.D., Gellert, S., Knauth, K., Pozniak, J., Peters, J., Dittmann, P., Mengoni, M., et al. (2023). CD4+ T cell-induced inflammatory cell death controls immune-evasive tumours. Nature *618*, 1033–1040.

67. Hollenbaugh, J.A., Reome, J., Dobrzanski, M., and Dutton, R.W. (2004). The Rate of the CD8-Dependent Initial Reduction in Tumor Volume Is Not Limited by Contact-Dependent Perforin, Fas Ligand, or TNF-Mediated Cytolysis. J. Immunol. *173*, 1738–1743.

68. Blomberg, O.S., Spagnuolo, L., Garner, H., Voorwerk, L., Isaeva, O.I., van Dyk, E., Bakker, N., Chalabi, M., Klaver, C., Duijst, M., et al. (2023). IL-5-producing CD4+ T cells and eosinophils cooperate to enhance response to immune checkpoint blockade in breast cancer. Cancer Cell *41*, 106–123.e10.

69. Linde, I.L., Prestwood, T.R., Qiu, J., Pilarowski, G., Linde, M.H., Zhang, X., Shen, L., Reticker-Flynn, N.E., Chiu, D.K.-C., Sheu, L.Y., et al. (2023). Neutrophil-activating therapy for the treatment of cancer. Cancer Cell *41*, 356–372.e10.

70. Chao, M.P., Majeti, R., and Weissman, I.L. (2011). Programmed cell removal: a new obstacle in the road to developing cancer. Nat. Rev. Cancer *12*, 58–67.

71. Lecoultre, M., Dutoit, V., and Walker, P.R. (2020). Phagocytic function of tumor-associated macrophages as a key determinant of tumor progression control: a review. J. Immunother. Cancer *8*, e001408.

72. Valgardsdottir, R., Cattaneo, I., Klein, C., Introna, M., Figliuzzi, M., and Golay, J. (2017). Human neutrophils mediate trogocytosis rather than phagocytosis of CLL B cells opsonized with anti-CD20 antibodies. Blood *129*, 2636–2644.

73. Sikic, B.I., Lakhani, N., Patnaik, A., Shah, S.A., Chandana, S.R., Rasco, D., Colevas, A.D., O'Rourke, T., Narayanan, S., Papadopoulos, K., et al. (2019). First-in-Human, First-in-Class Phase I Trial of the Anti-CD47 Antibody Hu5F9-G4 in Patients With Advanced Cancers. J. Clin. Oncol. *37*, 946–953.

74. Chen, S.-H., Dominik, P.K., Stanfield, J., Ding, S., Yang, W., Kurd, N., Llewellyn, R., Heyen, J., Wang, C., Melton, Z., et al. (2021). Dual checkpoint blockade of CD47 and PD-L1 using an affinity-tuned bispecific antibody maximizes antitumor immunity. J. Immunother. Cancer *9*, e003464.

75. Xu, L., Wang, S., Li, J., and Li, B. (2019). CD47/SIRPα blocking enhances CD19/CD3-bispecific T cell engager antibody-mediated lysis of B cell malignancies. Biochem. Biophys. Res. Commun. *509*, 739–745.

76. Fehsel, K., Kröncke, K.D., Meyer, K.L., Huber, H., Wahn, V., and Kolb-Bachofen, V. (1995). Nitric oxide induces apoptosis in mouse thymocytes. J. Immunol. *155*, 2858–2865.

77. Saio, M., Radoja, S., Marino, M., and Frey, A.B. (2001). Tumor-Infiltrating Macrophages Induce Apoptosis in Activated CD8+ T Cells by a Mechanism Requiring Cell Contact and Mediated by Both the Cell-Associated Form of TNF and Nitric Oxide. J. Immunol. *167*, 5583–5593.

78. Ridnour, L.A., Isenberg, J.S., Espey, M.G., Thomas, D.D., Roberts, D.D., and Wink, D.A. (2005). Nitric oxide regulates angiogenesis through a functional switch involving thrombospondin-1. Proc. Natl. Acad. Sci. USA *102*, 13147–13152.

79. Wang, M.M., Coupland, S.E., Aittokallio, T., and Figueiredo, C.R. (2023). Resistance to immune checkpoint therapies by tumour-induced T-cell desertification and exclusion: key mechanisms, prognostication and new therapeutic opportunities. Br. J. Cancer *129*, 1212–1224.

80. Ordentlich, P. (2021). Clinical evaluation of colony-stimulating factor 1 receptor inhibitors. Semin. Immunol. *54*, 101514.

81. Evans, T.J., Basu, B., Hubner, R., Ma, Y.T., Meyer, T., Palmer, D.H., Pinato, D.J.J., Plummer, E.R., Ross, P.J., Samson, A., et al. (2023). A phase I/II study of the CXCR2 inhibitor, AZD5069, in combination with durvalumab, in patients (pts) with advanced hepatocellular carcinoma (HCC). J. Clin. Oncol. *41*, TPS631.

82. Belkina, A.C., Ciccolella, C.O., Anno, R., Halpert, R., Spidlen, J., and Snyder-Cappione, J.E. (2019). Automated optimized parameters for T-distributed stochastic neighbor embedding improve visualization and analysis of large datasets. Nat. Commun. *10*. 5415. https://doi.org/10.1038/s41467-019-13055-y.

STAR★METHODS

KEY RESOURCES TABLE

REAGENT or RESOURCE	SOURCE	IDENTIFIER
Antibodies		
Purified CD16/CD32 (2.4G2)	BD Biosciences	Cat#: 553141; RRID: AB_394656
4-1BB – APC (17B5)	Biolegend	Cat#: 106110; RRID: AB_2564297
Arg-1 – PE/Cy7 (A1exF5)	Invitrogen	Cat#: 25-3697-82; RRID: AB_2734841
CCR2 – BV785 (SA203G11)	Biolegend	Cat#: 150621; RRID: AB_2721565
CCR2 – FITC (SA203G11)	Biolegend	Cat#: 150608; RRID: AB_2616980
CCR5 – APC (7A4)	ThermoFisher	Cat#: 17-1951-82; RRID: AB_2802223
CD3e – FITC (145-2C11)	Invitrogen	Cat#: 11-0031-85; RRID: AB_464883
CD3e – BV510 (145-2C11)	BD Biosciences	Cat#: 563024; RRID: AB_2737959
CD3e – PECF594 (145-2C11)	BD Biosciences	Cat#: 562286; RRID: AB_11153307
CD4 – BUV496 (RM4-5)	BD Biosciences	Cat#: 741050; RRID: AB_2870665
CD4 – BV605 (RM4-5)	Biolegend	Cat#: 100548; RRID: AB_2563054
CD8a – BUV395 (53–6.7)	BD Biosciences	Cat#: 565968; RRID: AB_2739421
CD8a – PerCP-Cy5.5 (53–6.7)	Biolegend	Cat#: 100734; RRID: AB_2075238
CD11b – BUV563 (M1/70)	BD Biosciences	Cat#: 741242; RRID: AB_2870793
CD11b – APC/Fire750 (M1/70)	Biolegend	Cat#: 101262; RRID: AB_2572122
CD11b – PE/Cy7 (M1/70)	Invitrogen	Cat#: 25-0112-82; RRID: AB_469588
CD11c – BV605 (HL3)	BD Biosciences	Cat#: 563057; RRID: AB_2737978
CD11c – APC/Fire750 (N418)	Biolegend	Cat#: 117352; RRID: AB_2572124
CD11c – APC/Cy7 (N418)	Biolegend	Cat#: 117324; RRID: AB_830649
CD19 – SparkBlue550 (6D5)	Biolegend	Cat#: 115566; RRID: AB_2832389
CD19 – BV510 (1D3)	BD Biosciences	Cat#: 562956; RRID: AB_2737915
CD19 – FITC (1D3)	Invitrogen	Cat#: 11-0193-82; RRID: AB_657666
CD25 – BV421 (PC61)	Biolegend	Cat#: 102043; RRID: AB_2562611
CD27 – BUV785 (LG.3A10)	Biolegend	Cat#: 124241; RRID: AB_2800595
CD28 – PE/Cy7 (37.51)	Biolegend	Cat#: 102126; RRID: AB_2617011
CD39 – PE (Duha59)	Biolegend	Cat#: 143804; RRID: AB_11218603
CD40 – BUV395 (3/23)	BD Biosciences	Cat#: 745697; RRID: AB_2743179
CD44 – BV510 (IM7)	Biolegend	Cat#: 563114; RRID: AB_2738011
CD44 – BV785 (IM7)	Biolegend	Cat#: 103059; RRID: AB_2571953
CD45 – Alexa Fluor 700 (30-F11)	Biolegend	Cat#: 103128; RRID: AB_493715
CD45.1 – Alexa Fluor 700 (A20)	Biolegend	Cat#: 110724; RRID: AB_493733
CD45.2 – APC-eFluor780 (104)	Invitrogen	Cat#: 47-0454-82; RRID: AB_1272175
CD47 – purified (miap301)	Biolegend	Cat#: 127502; RRID: AB_1089035
CD49a – BUV737 (Ha31/8)	BD Biosciences	Cat#: 741776; RRID: AB_2871130
CD54 – FITC (YN1/1.7.4)	ThermoFisher	Cat#: 11-0541-82; RRID: AB_465094
CD62L – BUV805 (MEL-14)	BD Biosciences	Cat#: 741924; RRID: AB_2871237
CD62L – BV421 (MEL-14)	Biolegend	Cat#: 104436; RRID: AB_2562560
CD69 – BUV737 (H1.2F3)	BD Biosciences	Cat#: 612793; RRID: AB_2870120
CD70 – BUV661 (FR70)	BD Biosciences	Cat#: 741564; RRID: AB_2870990
CD86 – BUV496 (PO3)	BD Biosciences	Cat#: 750437; RRID: AB_2874600
CD86 – BV650 (GL-1)	Biolegend	Cat#: 105036; RRID: AB_2686973
CD122 – PE/Cy5 (TM-β1)	Biolegend	Cat#: 123220; RRID: AB_2715962
CD163 – BV421 (S15049I)	Biolegend	Cat#: 155309; RRID: AB_2814063
CTLA-4 – BV421 (UC10-4B9)	Biolegend	Cat#: 106312; RRID: AB_2563063

(*Continued on next page*)

Continued

REAGENT or RESOURCE	SOURCE	IDENTIFIER
CXCL9 – PE (MIG-2F5.5)	Biolegend	Cat#: 515603; RRID: AB_2245489
Egr2 – APC (Erongr2)	Invitrogen	Cat#: 17-6691-82; RRID: AB_11151502
Egr2 – PE (Erongr2)	Invitrogen	Cat#: 12-6691-082; RRID: AB_10717804
Eomes – PE/eFluor610 (Dan11mag)	Invitrogen	Cat#: 61-4875-82; RRID: AB_2574614
F4/80 – PE/Cy5 (BM8)	Biolegend	Cat#: 123112; RRID: AB_893482
F4/80 – PE (BM8)	Biolegend	Cat#: 123110; RRID: AB_893486
FoxP3 – PacificBlue (MF-14)	Biolegend	Cat#: 126410; RRID: AB_2105047
Granzyme B – PerCP-Cy5.5 (QA16A02)	Biolegend	Cat#: 372212; RRID: AB_2728379
IL-12 – APC (C15.6)	Biolegend	Cat#: 505205; RRID: AB_315369
iNOS – Alexa Fluor 488 (CXNFT)	Biolegend	Cat#: 53-5920-82; RRID: AB_2574423
iNOS – APC (CXNFT)	Invitrogen	Cat#: 17-5920-82; RRID: AB_2573244
Ki-67 – BV605 (16A8)	Biolegend	Cat#: 652413; RRID: AB_2562664
KLRG1 – PerCP/Cy5.5 (2F1/KLRG1)	Biolegend	Cat#: 563595; RRID: AB_2738301
LTBR – PE (3C8)	Invitrogen	Cat#: 12-5671-82; RRID: AB_2016713
Ly6C – PerCP/Cy5.5 (HK1.4)	Biolegend	Cat#: 128012;; RRID: AB_1659241
Ly6C – BV605 (HK1.4)	Biolegend	Cat#: 128036; RRID: AB_2562353
Ly6G – SparkBlue550 (1A8)	Biolegend	Cat#: 127664; RRID: AB_2860671
Ly6G – APC/Fire750 (1A8)	Biolegend	Cat#: 127652; RRID: AB_2616733
Ly6G – BV785 (1A8)	Biolegend	Cat#: 127645; RRID: AB_2566317
I-A/I-E – PacificBlue (M5/114.15.2)	Biolegend	Cat#: 107620; RRID: AB_493527
I-A/I-E – BV510 (2G9)	BD Biosciences	Cat#: 743871; RRID: AB_2741822
NK1.1 – BV650 (PK136)	BD Biosciences	Cat#: 564143; RRID: AB_2738617
NK1.1 – BV510 (PK136)	Biolegend	Cat#: 108738; RRID: AB_2562217
NKG2A – PE/Cy7 (16A11)	Biolegend	Cat#: 142810; RRID: AB_2728161
OX-40 (CD134) – BV711 (OX-86)	Biolegend	Cat#: 119421; RRID: AB_2687176
PD-1 – BV605 (29F.1A12)	Biolegend	Cat#: 135220; RRID: AB_2562616
PD-L1 – BUV737 (MIH5)	BD Biosciences	Cat#: 741877; RRID: AB_2871203
PD-L1 – BV421 (MIH5)	BD Biosciences	Cat#: 564716; RRID: AB_2738911
Siglec-F – BV711 (E50-2440)	BD Biosciences	Cat#: 740764; RRID: AB_2740427
Siglec-G – BUV615 (SH1)	BD Biosciences	Cat#: 751581; RRID: AB_2875576
Siglec-H – BV650 (440c)	BD Biosciences	Cat#: 747672; RRID: AB_2744233
SIRPα – APC/Cy7 (P84)	Biolegend	Cat#: 144018; RRID: AB_2629558
T-bet – BV711 (4B10)	Biolegend	Cat#: 644820; RRID: AB_2715766
TCF1/7 – Alexa Fluor 647 (812145)	R&D Systems	Cat#: FAB8224R; RRID: AB_2888931
TIGIT – PE/Dazzle594 (1G9)	Biolegend	Cat#: 142110; RRID: AB_2566573
Tim-3 – BV785 (RMT3-23)	Biolegend	Cat#: 119725; RRID: AB_2716066
XCR1 – PE (ZET)	Biolegend	Cat#: 148204; RRID: AB_2563843
Tetramer – APC (Abu-Abu-Abu-L-Abu-L-T-V-F-L)	Immudex	N/A
*InVivo*Plus anti-mouse CD4	BioXCell	Cat#: BP0003-1; RRID: AB_1107636
*InVivo*Plus anti-mouse CD8α	BioXCell	Cat#: BP0061; RRID: AB_1125541
*InVivo*Plus anti-mouse CSF1R (CD115)	BioXCell	Cat#: BP0213; RRID: AB_2687699
*InVivo*Plus anti-mouse Ly6G	BioXCell	Cat#: BP0075-1; RRID: AB_1107721
*InVivo*Plus anti-mouse NK1.1	BioXCell	Cat#: BP0036; RRID: AB_1107737
*InVivo*Plus anti-mouse PD-L1	BioXCell	Cat#: BP0101; RRID: AB_10949073
*InVivo*MAb anti-mouse IFNγ	BioXCell	Cat#: BE0055; RRID: AB_1107694
*InVivo*MAb anti-mouse IFNγR	BioXCell	Cat#: BE0029; RRID: AB_1107576
Rat anti-mouse CD8 (4SM15)	eBioscience	Cat#: 14-0808-82; RRID: AB_2572861
Rabbit anti-mouse iNOS (PA3-030A)	ThermoFisher	Cat#: PA3-030A; RRID: AB_2152737
Rabbit anti-mouse F4/80 (D2S9R)	Cell Signaling	Cat#: 70076; RRID: AB_2799771

(*Continued on next page*)

Continued

REAGENT or RESOURCE	SOURCE	IDENTIFIER
Rabbit anti-rat IgG	Abcam	Cat#: ab6733; RRID: AB_954909
Donkey anti-rabbit IgG (H + L) Alexa Fluor 555	ThermoFisher	Cat#: A-31572; RRID: AB_162543
Goat anti-rat IgG (H + L) Alexa Fluor 488	ThermoFisher	Cat#: A48262; RRID: AB_2896330
Mouse T-Activator CD3/CD28 Dynabeads	ThermoFisher	Cat#: 11-452-D
Chemicals, peptides, and recombinant proteins		
Recombinant Murine M-CSF	Peprotech	Cat#: AF-315-02-B
Recombinant IL-2	Peprotech	Cat#: 212-12
Recombinant Murine IL-7	Bio-Techne	Cat#: 407-ML
Lipopolysaccharides from Escherichia coli O26:B6	Sigma Aldrich	Cat#: L8274
Recombinant Mouse IFN-γ	Biolegend	Cat#: 575308
Sodium Chloride	Sigma Aldrich	Cat#: S5886
Liberase TL Research grade	Roche	Cat#: 05401020001
RMA Env-encoded CD4 T cell epitope (EPLTSLTPRCNTAWNRLKL)	Peptide synthesis facility of department IHB, LUMC	N/A
RMA Gag-encoded CD8 T cell epitope (CCLCLTVFL)	Genscript	Cat#: SC1208 Chemical Peptide
CpG (ODN 1826)	Invivogen	Cat#: tlrl-1826
$OVA_{241-270}$ peptide (SMLVLLPDEVSGLEQLESIINFEKLTEWTS)	Peptide synthesis facility of department IHB, LUMC	N/A
CD3xTRP1 bsAb	Genmab	N/A
Recombinant human IL-2	Clinigen	N/A
Aldara crème (5% Imiquimod)	3M Pharmaceuticals	N/A
Entellan mouting medium for microscopy	Sigma Aldrich	Cat#: 107960
PAP pen for immunostaining	Merck Millipore	Cat#: Z377821
Microscope slides, SuperFrost Plus	VWR	Cat#: 631-0108
Hirschmann™ Glass covers	ThermoFisher	Cat#: 10329241
Hydrogen peroxide 30%	Merck Millipore	Cat#: 107209
Methanol >98.5%	VWR Chemicals	Cat#: 20903.415
Tri-sodium Citrate Dihydrate	Merck	Cat#: 106448
SuperBlock™ (PBS) Blocking Buffer	ThermoFisher	Cat#: 37515
DAPI (4′,6-Diamidino-2-Phenylindole, Dihydrochloride)	ThermoFisher	Cat#: D1306
Bovine Serum Albumin (BSA)	Sigma Aldrich	Cat#: A3912
Tween 20	Merck	Cat#: 8221840500
Mayer's haematoxylin staining	Merck	Cat#: 1092490500
DAB^+ Substrate Chromogen System (Dako Omnis)	Agilent	Cat#: GV825
L-arginine ≥98%	Sigma-Aldrich	Cat#: A5006
RPMI 1640 Medium for SILAC	ThermoFisher	Cat#: 88365
Maraviroc	Tocris	Cat#: 3756
LTBR blocking peptide	Abcepta	Cat#: BP16019a
Tak-242	Tocris	Cat#: 6587
E6446	SelleckChem	Cat#: S0716
Cu-CPT22	SelleckChem	Cat#: S8677
Percoll	GE Healthcare	Cat#: 17-0891-01
96 Well EIA/RIA Assay Microplate	Corning	Cat#: CLS3590
Purified Rat Anti-Mouse IFN-γ	BD Biosciences	Cat#: 551216; RRID: AB_394094
Biotin Rat Anti-Mouse IFN-γ	BD Biosciences	Cat#: 554410; RRID: AB_395374
Streptavidin/Avidin multi-labeled HRP	Sanquin	Cat#: M2051
Recombinant Mouse IFN-γ	BD Biosciences	Cat#: 554587; RRID: AB_2868979
3,3′,5,5′-Tetramethylbenzidine (TMB)	Sigma Aldrich	Cat#: T0440
Sodium carbonate decahydrate	Merck	Cat#: 106391

(*Continued on next page*)

Continued

REAGENT or RESOURCE	SOURCE	IDENTIFIER
Sodium hydrogen carbonate	Merck	Cat#: 106329
Sulfuric acid 95–97%	Merck	Cat#: 100731
TNF-alpha/TNFA/TNFSF2 Neutralizing Antibody	SinoBiological	Cat#: 50349-RN023
DETA NONOate (Noc18)	MedChemExpress	Cat#: HY-136278
Critical commercial assays		
Zombie UV fixable viability kit	Biolegend	Cat#: 423108
LIVE/DEAD™ Fixable Aqua Dead Cell Stain Kit	ThermoFisher	Cat#: L34957
FoxP3/Transcription Factor Staining Buffer Set	Invitrogen	Cat#: 00-5523-00
VECTASTAIN® Elite ABC-HRP Kit	Vector Labs	Cat#: PK-6100; RRID: AB_2336819
CellTrace™ CFSE Cell Proliferation Kit	ThermoFisher	Cat#: C34554
Griess Reagent Kit	ThermoFisher	Cat#: G7921
Mouse CD8 T Lymphocyte Enrichment Set	BD Biosciences	Cat#: 558471
Dynabeads flowcomp CD8 kit	Thermo Fisher Scientific	Cat#: 11462D
Mouse CCL3/MIP-1 alpha DuoSet ELISA	R&D Systems	Cat#: DY450
Mouse CCL4/MIP-1 beta DuoSet ELISA	R&D Systems	Cat#: DY451
Mouse CCL5/RANTES DuoSet ELISA	R&D Systems	Cat#: DY478
nCounter PanCancer Immune Profiling cartridge	Nanostring	Cat#: 115000142
nCounter Myeloid Innate Immunity Panel V2	Nanostring	Cat#: XT-CSO-MMII2-12
NucleoSpin RNA mini kit for RNA purification	Macherey-Nagel	Cat#: 740955.50
High-Capacity RNA-to-cDNA™ Kit	ThermoFisher	Cat#: 4387406
Deposited data		
Raw and processed scRNA-seq data from MHC-II^{+} and MHC-II^{-} intratumoral (RMA-Qa1$^{-/-}$) murine macrophages	This manuscript	GEO: GSE263235
Raw and processed scRNA-seq data from intratumoral (CT26) murine macrophages	Qu, Y. et al.[42]	GEO: GSE150970
Raw and processed scRNA-seq data from human monocyte/macrophage populations across tissues	Mulder, K. et al.[43]	GEO: GSE178209
Raw and processed scRNA-seq data from human monocyte/macrophage and T cell populations in breast cancer	Bassez, A. et al.[48]	EGA: EGAS00001004809
Experimental models: Cell lines		
RMA	Dr. K. Kärre	RRID: CVCL_J385
B16F10	ATCC	Cat#: CRL6475 RRID: CVCL_0159
KPC3	Dr. F. Balkwill	RRID: CVCL_A9ZK
Experimental models: Organisms/strains		
Mouse C57BL/6J	Charles River Laboratories France	RRID: IMSR_JAX:000664
Mouse TCR transgenic gp100$_{25\text{-}33}$/H-2D^{b} bred to express congenic marker CD45.1 (Ly5.1)	Provided by Dr. N.P. Restifo (NIH, Bethesda, USA)	N/A
B6.129P2-*Nos2*^{tm1Lau}/J (iNOS$^{-/-}$)	The Jackson Laboratory	RRID: IMSR_JAX:002609
Oligonucleotides		
See Table S3.		
Software and algorithms		
FlowJo v10	Treestar	RRID: SCR_008520
OMIQ	Omiq Inc.	Omiq.ai
GraphPad Prism V9	GraphPad	RRID: SCR_002798
ImageJ	ImageJ	RRID: SCR_003070
InForm analysis software V2.6	Perkin Elmer	RRID: SCR_019155
Photoshop v2022	Adobe	RRID: SCR_014199
nSolver analysis software	Nanostring	RRID: SCR_003420
10x Genomics Cell Ranger software v7.0.0	10xgenomics	RRID: SCR_023672

(*Continued on next page*)

Continued

REAGENT or RESOURCE	SOURCE	IDENTIFIER
R v4.2.3	R	RRID: SCR_001905
GSEA v4.3.2	Broad Institute	RRID: SCR_003199
BioRender	BioRender	RRID: SCR_018361

RESOURCE AVAILABILITY

Lead contact

Further information and requests for resources and reagents should be directed to the lead contact Sjoerd van der Burg (shvdburg@lumc.nl).

Materials availability

This study did not generate new unique reagents.

Data and code availability

- scRNA-seq data have been deposited at GEO and are publicly available as of the date of publication. Accession numbers and DOI are listed in the key resources table.
- Additional microscopy data reported in this paper will be shared by the lead contact upon request.
- Any additional information required to reanalyze the data reported in this paper is available from the lead contact upon request.

EXPERIMENTAL MODEL AND STUDY PARTICIPANT DETAILS

Mice

C57BL/6J (BL/6J) mice (age 8–10 weeks, male) were obtained from Charles River Laboratories (France). TCR transgenic mice (age 8–12 weeks, male) containing $gp100_{25\text{-}33}$/H-2Db specific receptors were bred to express the congenic marker CD45.1 (Ly5.1) and were a kind gift from Dr. N.P. Restifo (NIH, Bethesda, USA). B6.129P2-*Nos2*^{tm1Lau}/J (iNOS$^{-/-}$) mice (age 8–14 weeks, male) were obtained from The Jackson Laboratory (U.S.A). All animals were housed in individually ventilated cages under specified pathogen-free conditions in the animal facility of the Leiden University Medical Center. All tumor outgrowth experiments were performed in C57BL/6J and/or iNOS$^{-/-}$ animals, while for the TME studies of the RMA-Qa1$^{b-/-}$ tumors Ly5.1 animals were used. All mouse experiments were controlled by the animal welfare committee (IvD) of the Leiden University Medical Center and approved by the national central committee of animal experiments (CCD) under the permit numbers AVD1160020197864 and AVD1160202010004 in accordance with the Dutch Act on Animal Experimentation and EU Directive 2010/63/EU.

Tumor cell lines

RMA-Qa1$^{b-/-}$ is a Raucher MuLV-induced T cell lymphoma RBL-5 cell line, generated by the CRISPR-Cas9-induced knock-out of the Qa-1^{b} gene. For the establishment of a homogeneous Qa1^{b} knockout cell line, cells were incubated for 48 h with 30 IU/mL IFN-γ (Biolegend) and subsequently sorted three times on Qa1^{b-} cells by flow cytometry.[17] RMA-Qa1$^{b-/-}$ and B16F10 (B16) cells were cultured in Iscove's modified Dulbecco's medium (IMDM; Invitrogen) supplemented with 8% (RMA-Qa1$^{b-/-}$) or 5% (B16) Fetal Calf Serum (FCS; Greiner), 100 IU/mL Penicillin/Streptomycin (Gibco) and 2 mM glutamin (Gibco) at 37°C and 5% CO_2. A low and constant passage number was used in all experiments and cell lines were regularly assured to be Mycoplasma negative by PCR analysis. Authentication of the cell lines was ensured by IDEXX bioanalytics using short tandem repeat markers (B16) or antigen-specific T cell recognition (RMA-Qa1$^{b-/-}$).

METHOD DETAILS

Treatment

Animals were subcutaneously inoculated with $1*10^3$ RMA-Qa1$^{b-/-}$ or $5*10^4$ B16F10 tumor cells in 200μL PBS containing 0.1% bovine serum albumin (BSA) on day 0 in the right, or right and left flank. For TME studies, mice were inoculated with $1.5*10^5$ B16F10 tumor cells. Tumor volume (l*w*h) was measured thrice weekly using a caliper. Animals were randomized based on tumor volume prior to treatment and experimental measurements were conducted in a blinded manner. Mice bearing RMA-Qa1$^{b-/-}$ tumors were treated with therapeutic vaccination when tumors reached a size of 10-50 mm^3. The peptide vaccine, containing 50 nmol of the Gag-encoded CD8$^+$ T cell epitope (CCLCLTVFL) and 20 nmol of the murine leukemia virus Env-encoded CD4$^+$ T cell epitope (EPLTSLTPRCNTAWNRLKL), supplemented with 20 μg CpG (ODN1826, InvivoGen), was dissolved in 50 μL PBS, and administered subcutaneously in the tail-base. For the prime-boost setting, animals received an additional vaccination at the tail-base 11 days after initial vaccination. Mice bearing B16F10 tumors were anesthetized using a mixture of xylazine and ketamine in 100 μL PBS via i.p. injection and immunized s.c. in the contralateral

flank with 150 μg chicken ovalbumine $OVA_{241-270}$ peptide (SMLVLLPDEVSGLEQLESIINFEKLTEWTS) in 100 μL PBS. Immediately following peptide injection, 60 mg of 5% imiquimod containing cream Aldara (3M Pharmaceuticals) was topically applied on the skin of the injection site. On the day of the second immunization and one day later, $6*10^5$IU recombinant human IL-2 was injected i.p. in 100 μL PBS, followed by i.p. injection of 12.5 μg CD3xTRP1 bsAb two days and five days after the second immunization. For RMA-Qa1$^{b-/-}$, NK cells and $CD8^+$ T cells were depleted by intraperitoneal injection of 200 μg α-NK1.1 depleting antibody (clone PK136, BioXCell) or 100 μg α-CD8α depleting antibody (clone 2.43, BioXCell) at day 11, 17, 24 and 31. Neutrophils and macrophages were depleted by intraperitoneal injection of 100 μg α-Ly6G depleting antibody (clone 1A8, BioXCell) at day 8 and 50 μg at day 10, 12, 14 and 18 and by 1 mg α-CD115 depleting antibody (clone AFS98, BioXCell) at day 8 and 300 μg at day 10, 12, 14, 16 and 18, respectively. For B16, NK cells were depleted at day 8, 11, 19 and 25. $CD8^+$ and $CD4^+$ T cells were depleted by intraperitoneal injection of 100 μg α-CD8α and α-CD4 (clone YTS177, BioXCell) at day 13 and 100 μg α-CD8α or 40 μg α-CD4 at day 16 and 18. For neutrophil and macrophage depletion, 100 μg α-Ly6G or 1 mg α-CD115 was administered at day 9, followed by 50 μg α-Ly6G at day 11, 15 and 18 or 300 μg α-CD115 at day 11, 13, 15, 17 and 19. Depletion efficiency for all depletion studies was checked by flow cytometry of blood immune cells at day 12. CCR5 signaling was inhibited by intraperitoneal injection with the selective CCR5 antagonist Maraviroc (Tocris) at 10 mg/kg. Treatment was started one day prior to therapeutic vaccination and continued daily for a total of 10 injections. LTBR function was inhibited by intraperitoneal injection of 100 μg α-LTBR blocking peptide at day 11 (abcepta). PD-1/PD-L1 interaction was blocked by intraperitoneal injection of 200 μg α-PD-L1 antibody (clone 10F.9G2, BioXCell) at day 9, 12, 15 and 19. For TME studies animals were euthanized around day 19, a timepoint at which clinical responses were visible. For survival studies animals were euthanized when tumors reached a size of 1000 mm^3 (unilateral model) or a combined volume of 1500 mm^3 (bilateral model).

Flow cytometry

For TME studies, tumors were collected and processed by physical digestion using razor blades and RMA-Qa1$^{b-/-}$ tumors were then chemically digested with Liberase TL (2.5 mg/mL, Roche) for 10 min as 37°C. Tumors were further processed into single-cell suspensions by using 70 μm cell strainers (BD Biosciences) and resuspended in PBS. Mouse Fc-receptors were blocked by Rat Anti-Mouse CD16/CD32 (Clone 2.4G2, BD) in PBS for 10 min at 4°C. Viability was assessed with the Zombie UV Fixable Viability Kit (Biolegend) or the LIVE/DEAD Fixable Aqua Dead Cell Stain Kit in PBS for 10 min at room temperature (RT) before surface staining. APC-conjugated tetramers (Abu-Abu-Abu-L-Abu-L-T-V-F-L) were added to the surface mix for the detection of GagL-specific $CD8^+$ T cells responses. Surface staining was performed in PBS supplemented with 0.5% BSA +0.02% Sodium azide (FACS buffer) for 20 min at 4°C. Subsequently, cells were fixed and permeabilized for intracellular marker staining using the FoxP3/Transcription Factor Staining Buffer Set (eBioscience) according to manufacturer's protocol. Following intracellular staining, cells were resuspended in FACS buffer and acquired on the Aurora 5L spectral flow cytometer (Cytek) or the LSR-II (BD Biosciences). Data was analyzed using FlowJo (Tree Star) for percentages and phenotype of intratumoral immune cells or using OMIQ data analysis software for the visualization of opt-SNE plots and wishbone trajectory analysis.[82]

Immunohistochemistry

Tumors were isolated from mice and directly fixed in formalin, followed by embedding in paraffin. Embedded tumors were sliced into 4 μm sections and mounted on adhesive slides. Sections were then deparaffinized and rehydrated, after which endogenous peroxidase activity was blocked with 0.3% hydrogen peroxidase solution (Merck Millipore) in methanol for 20 min. Antigen retrieval was performed in 0.01M Sodium Citrate solution (Merck Millipore, pH 6.0) in the microwave for 10 min. Non-specific binding of the primary antibody was reduced by SuperBlock (PBS) Blocking Buffer (ThermoFisher) at room temperature for 30 min. Tumor slides were incubated with rat anti-mouse CD8 (clone 4SM15, eBioscience) antibody diluted in PBS at 4°C overnight. Slides were then washed (0.05% Tween in PBS) and incubated with biotinylated Rabbit anti-rat IgG (Abcam) at room temperature for 1 h. Biotinylated antibody was labeled using the VECTASTAIN Elite ABC-HRP Kit (Vector Labs) according to manufacturer's protocol. Nuclear counterstaining was performed with filtered Mayer's Haematoxylin staining (ThermoFisher) at room temperature for 10–15 s. Antibody binding was detected with the Liquid DAB+ substrate chromogen system (DAKO, Agilent) and cell counts were quantified using ImageJ software. On all immunohistochemistry pictures a photo correction of +200% saturation, −20% brightness and +40% contrast was applied.

Immunofluorescence

The spectral immunofluorescence panels used were CD8, F4/80 and DAPI, and CD8, iNOS and DAPI. Antibody specificity was confirmed by immunohistochemistry. Fixation, embedding, deparaffinization, antigen retrieval and blocking of non-specific binding was identical to immunohistochemistry staining. Tumor slides were then incubated with rat anti-mouse CD8 (clone 4SM15, eBioscience) and rabbit anti-mouse iNOS (PA3-030A, ThermoFisher) or rabbit anti-mouse F4/80 (D2S9R, Cell Signaling) antibodies diluted in PBS at room temperature overnight. Slides were then washed (0.05% Tween in PBS) and incubated with donkey anti-rabbit IgG (H + L) Alexa Fluor 555 (Invitrogen) or goat anti-rat IgG (H + L) Alexa Fluor 488 (Invitrogen) highly cross-absorbed secondary antibody diluted in PBS for 60 min at room temperature in the dark. Nuclear counterstaining was performed with DAPI (ThermoFisher) for 15 min at room temperature in the dark. Immunofluoresence images were acquired using the Vectra 3.0.5 multispectral imaging microscope (PerkinElmer) at 20× magnification. InForm analysis software version 2.6 (PerkinElmer) was used for spectral unmixing. Per treatment group the number of F4/80+ or iNOS+ cells within a 60 pixel radius of a $CD8^+$ cells was quantified using Photoshop, with a minimum of 800 CD8 cells per group.

ELISA

$CD8^+$ T cells were enriched from splenocytes using the Mouse CD8 T cell Lymphocyte Enrichment Set (BD Biosciences) or from vacc. + bsAb treated B16 tumors by cell sorting (Live, $CD45^+$, $CD3^+$, $CD8^+$) on the BD Aria cell sorter and collected at a purity >90%. $1*10^6$ $CD8^+$ T cells were seeded in complete IMDM supplemented with 20 IU/mL IL-2 in 6-wells flat-bottom culture plates and activated with CD3/CD28 dynabeads (ThermoFisher). After 24 h, supernatant from unstimulated or CD3/CD28-stimulated $CD8^+$ T cells was collected. CCL3, CCL4 and CCL5 cytokine production was determined by DuoSet ELISAs (R&D Systems). For the determination of IFN-γ production by $CD8^+$ T cells, 96-wells flat bottom ELISA plates were coated with 1 μg/mL rat anti-mouse IFN-γ antibody (clone R4-6A2, BD Biosciences) in coating buffer containing sodium carbonate and sodium bicarbonate (Merck) at pH 9.6 overnight at 4°C. Following all incubation steps, plates were washed thrice by PBS +0.05% Tween 20 (washing buffer). Next, plates were incubated for 1 h with washing buffer +1% BSA (blocking buffer) at 37°C and 5% CO_2, after which samples and IFN-γ standard (BD Biosciences) were added to the plates and incubated for 2 h at room temperature. After 2 h, plates were incubated first with 0.5 μg/mL biotin-labeled rat anti-mouse IFN-γ (clone XMG1.2, BD Biosciences) and then with 1/10000 Streptavidin/Avidin multi-labeled HRP (Sanquin) subsequently for 1 h at room temperature. Finally, 50 μL Tetramethyl-benzidine liquid substrate (TMB, Sigma Aldrich) was added to the plates and the reaction was stopped by adding 50 μL 2M H_2SO_4 (Merck) in MilliQ (Braun) to the plate. Optical density of all ELISAs was measured at 450 nm in a spectrophotometer and cytokine production was determined relative to the standard solutions.

Transcriptomics

For transcriptomic analysis, untreated and treated RMA-Qa1$^{b-/-}$ or KPC3-TRP1 tumors were harvested and processed into single cell suspensions as described above. Treated RMA-Qa1$^{b-/-}$ tumors were further categorized based on their change in tumor volume into responders (decrease in tumor volume) or non-responders (increase in tumor volume). Total RNA was isolated from single cell suspensions using the NucleoSpin RNA kit (Macherey-Nagel) according to manufacturer's protocol. The total RNA quality and yield after sample preparation were determined using the DNF-474 HS NGS Fragment Kit (Agilent) and analyzed using the Fragment Analyzer. The resulting products were consistent with 95% of the fragments >300 bp. RNA (300 ng/sample) was loaded on nCounter Myeloid Innate Immune or nCounter PanCancer Immune Profiling (Nanostring) cartridges and the fluorescent barcodes were measured on the nCounter Analysis System (NanoString) according to the manufacturer's instructions. Data were processed and normalized using nSolver Analysis Software (V4.0) and the Advanced Analysis module (V.2.0, NanoString). NanoString-defined markers were used to analyze cell type scores and immune pathways. Benjamini-Hochberg correction for multiple comparisons was used to minimize the false-discovery rate.

Single cell RNA-sequencing

For single cell RNA sequencing (scRNA-seq) mice bearing RMA-Qa1$^{b-/-}$ tumors were treated with therapeutic vaccination when tumors reached a size of 10-50 mm^3. At time of regression, tumors were harvested and processed into single cell suspensions as described above. From single cell suspensions $MHCII^+$ and $MHCII^-$ macrophages (Live, $CD45^+$, $CD11b^+$, $F4/80^+$) were sorted using the BD Aria cell sorter and collected at a purity >90%. Sample quality control and scRNA-seq were both performed by the Leiden Genome Technology Center of the Leiden University Medical Center. Single cell gene expression libraries were generated on the 10x Genomics Chromium X platform using the Chromium Next GEM Single Cell 3′ Library & Gel Bead Kit v3.1 and Chromium Next GEM Chip G Single Cell Kit (10x Genomics) according to the manufacturer's protocol. Gene expression libraries were sequenced on a NovaSeq 6000 S4 flow cell using v1.5 chemistry (Illumina) and fastq files were generated using Cell Ranger mkfastq (10x Genomics). Fastq files were analyzed with the 10x Genomics Cell Ranger software v7.0.0 and the mouse mm10 reference using default settings.

All downstream analysis was performed using Seurat (v.4.3.0). Raw data was merged and cells with a low number of expressed genes (<500) were filtered out from the analysis, resulting in a final dataset of 37,047 cells. Merged data were normalized using Seurat's 'LogNormalize' function with a scaling factor set at 10,000. Variable features were identified using the 'FindVariableFeatures' function, resulting in the selection of 2,000 features. For the visualization of cells in a two-dimensional space, t-distributed stochastic neighbor embedding (t-SNE) was employed. Differential gene expression analysis was performed using the 'FindAllMarkers' function, with min.pct and logfc.threshold at 0.25. The top 10 most differentially expressed genes per cluster, based on logfc, were plotted in a heatmap using 'DoHeatmap' and selected genes of interests were visualized in a dotplot using 'DotPlot'. Trajectory analysis was conducted utilizing monocle3 (v1.3.1), SeuratWrappers (v0.3.1), and patchwork (v1.1.2). The 'RunUMAP' function was used to perform dimensionality reduction and construct Uniform Manifold Approximation and Projection (UMAP) plots. The Seurat object was converted to a 'cell_data_set' object to allow integration of the Seurat data into the Monocle3 analysis framework. A trajectory graph was learned from the data using the 'learngraph' function, with partition-based grouping utilized for graph construction. Subsequently, cells were ordered along the learned trajectory using the 'order_cells' function. Cells corresponding to cluster 5 were chosen as root cells for ordering. The function 'plot_cells' was used to visualize the ordered trajectory by coloring cells based on pseudotime. Gene set enrichment analysis (GSEA) was performed using the GSEA v4.3.2 software (Broad Institute) on the pre-ranked DEGs from macrophage cluster 3. Mus musculus gene ontology biological process gene sets (m5.go.bp.v2023.1.Mm) were selected for the enrichment. Gene set permutations were performed 1000 times for the analysis, followed by the verification of the top 15 enriched pathways based on the normalized enrichment score (NES) and false discovery rate (FDR).

Percentual overlap and Spearman correlation were determined for the top 50 DEGs from the clusters C0-9 of our scRNA-seq dataset compared to macrophage cluster M3 from GSE150970, for which a positive association with the response to PD-L1 blockade in CT26 tumors was demonstrated.[42]

The macrophage signature was computed using the top 100 differentially expressed genes in the macrophage (C3) cluster identified from the analysis of the mouse single-cell RNA sequencing data and used to compare to bulk RNA-seq data from two cohorts of patients with melanoma. The patients were part of the University of Chicago IRB protocols 15–0837 and 14–0735 and received one of the following α-PD-1-based immunotherapies: Pembrolizumab, Ipilimumab+Nivolumab, Nivolumab, Nivolumab+CD137, Nivolumab+IDO, PD.1+GITR, Nivolumab+IDO, Pembrolizumab+IDO, Pembrolizumab+IDO+IL2, Pembrolizumab+RANK or Pembrolizumab+STAT3 and had a recorded clinical outcome. All samples were sequenced using HiSeq4000 and abundances of transcripts from the bulk RNA sequencing data were quantified using *Kallisto* software. Sequencing samples collected prior to the first immunotherapy dose were selected. Out of the 60 total patients, 8 were classified as complete response, 19 as partial response, 19 as stable disease, and 14 as progressive disease.

Preprocessing of the data involved removing genes with a maximum median count lower than 2^4 (the maximum median for each gene was defined as the maximum of the four median counts of a gene calculated for each of the four clinical outcomes). The filtering threshold was chosen such that the filtered counts had a bimodal distribution. Data was then normalized using the *variance stabilizing transformation* function from the *DESeq2* package. Data was corrected for batch effects using the *ComBat-Seq* package (two batches were identified due to high differences in the total number of transcripts). Subsequently, the mouse genes from the macrophage C3 cluster were converted into their human orthologs using the *BiomaRt* package. Using the normalized data, a single sample Gene Set Enrichment score (ssGSEA) was computed for the macrophage gene list using the *GSVA* package. Samples were split in two different groups, responders (patients classified as complete response, partial response, and stable disease) and non-responders (patients classified as progressive disease).

The publicly available scRNA-seq dataset from Mulder et al.[43] was downloaded from the FG Lab Resources platform (https://gustaveroussy.github.io/FG-Lab/). Macrophage clusters were extracted from the annotated MoMacVERSE dataset. UMAPs were plotted using the original UMAP coordinates provided by the authors as stored in the Seurat object. ssGSEA was performed using the macrophage gene list (murine C3 macrophage signature) using the *GSVA* package, and the resulting enrichment scores were overlayed on the UMAP using *ggplot2* (v 3.4.4). A stacked barchart was plotted to visualize proportions of total macrophage count by tissue (cancer type) and status (Cancer/Healthy/Other) using *ggplot2* (v2.3.4.2). The DEGs for human Mulder macrophage cluster #6 were obtained from the supplementary material from the original publication.[43] Gene set enrichment analysis (GSEA) was performed using the GSEA v4.3.2 software (Broad Institute) on the pre-ranked DEGs from human Mulder macrophage cluster #6. Homo sapiens gene ontology biological process gene sets (c5.go.bp.v2023.2.Hs) were selected for the enrichment. Gene set permutations were performed 1000 times for the analysis, followed by the verification of the top 10 enriched pathways based on the normalized enrichment score (NES) and false discovery rate (FDR).

The publicly available scRNA-seq dataset from Bassez et al.[48] was downloaded from the data access page of the Lambrechts lab website (https://lambrechtslab.sites.vib.be/en/single-cell). The downloaded monocyte/macrophage (n = 7,952 cells) count matrix and T cell matrix (n = 53,382 cells) and corresponding metadata were converted into Seurat objects using R. Downstream analysis was performed using Seurat (v.4.3.0). Data were normalized using the LogNormalize function of Seurat with a scale factor of 10,000. Variable features were identified using the FindVariableFeatures function of Seurat returning 2,000 features. t-SNE was used to visualize the cells in a two-dimensional space. ssGSEA was performed to compute gene set enrichment scores for the human Mulder cluster #6 macrophage signature obtained from the MoMacVERSE dataset and for the murine-derived C3 macrophage signature, resulting scores were overlayed on the monocyte/macrophage t-SNE. Clusters of monocytes/macrophages were identified by a shared nearest neighbor (SNN) modularity optimization-based clustering, the FindNeighbors and FindClusters functions of Seurat were applied. To compare enrichment scores between these clusters, violin plots were generated using *ggplot2*. The relative proportions of the distinct monocyte/macrophage clusters were compared between patients with T cell expansion following α-PD-1 treatment (responders) and those without T cell expansion (non-responders) for pre-treatment and on-treatment samples using a Mann-Whitney *U*-test. Data was represented as boxplots using *ggplot2*. Gene set enrichment analysis (GSEA) was performed using the GSEA v4.3.2 software (Broad Institute) on the pre-ranked DEGs from human macrophage cluster 0. Homo sapiens gene ontology biological process gene sets (c5.go.bp.v2023.2.Hs) were selected for the enrichment. Gene set permutations were performed 1000 times for the analysis, followed by the verification of the top 15 enriched pathways based on the normalized enrichment score (NES) and false discovery rate (FDR).

$CD8^+$ and $CD4^+$ T cell clusters, as defined by Bassez et al.,[48] were extracted from the T cell Seurat object (n = 48,315 cells). t-SNE was used to visualize the distinct clusters in relation to treatment response. The relative proportions of these T cell clusters were compared between "biological" responders and non-responders using a Mann-Whitney *U*-test and represented by boxplots. *CCL3*, *CCL4*, and *CCL5* expression values were overlayed on the tSNE and were visualized in a dotplot using the Seurat function 'DotPlot' to compare expression between the defined clusters. The abundance of each cell populations was calculated as a percentage of the total cells per sample. To determine the relation between presence of the defined macrophage population and these CCL3, CCL4, and CCL5 positive T cells, the Spearman correlation was calculated between the percentage of cluster 0 macrophages and the percentage of experienced $CD4^+$ and $CD8^+$ T cells. Results were visualized in a scatterplot using *ggplot2*.

BMDM and co-culture assays

Bone marrow was isolated from tibia en femurs and processed into single-cell suspensions using 70 μm cell strainers (BD Biosciences). To exclude resident macrophages from analysis, single cell suspensions were transferred to 100/20 mm culture dishes and cultured in full RPMI for 4 h at 37°C and 5% CO_2. After 4 h, non-adherent cells were collected and plated at a density of 1,5*10^6 cells/mL in 6-wells tissue culture plates. After 24 h, M-CSF (20 ng/mL, Invitrogen) was added to cell cultures and refreshed every other day. Macrophage purity was >90%, as assessed by CD11b and F4/80 staining by flow cytometry. After six days of differentiation, BMDMs were skewed for 24 h in high-salt culture medium (full RPMI +40 mM/mL NaCl) to mimic the physiological conditions of the tumor. To pre-skew classical M1 macrophages, IFN-γ (20 ng/mL, Invitrogen) and LPS (100 ng/mL, Sigma Aldrich) were added to the culture systems. To assess the effect of $CD8^+$ T cells on macrophage skewing, $CD8^+$ T cells were isolated from splenocytes of naive or RMA-Qa1$^{b-/-}$ tumor-bearing vaccinated mice using a mouse CD8 T lymphocyte enrichment kit (BD Biosciences) according to the manufacturer's instructions. Alternatively $CD8^+$ T cells were isolated from vacc. + bsAb treated B16F10 tumors by gradient centrifugation of the single cell tumor suspension using 44% and 66% Percoll solutions (GE Healthcare), followed by CD8 enrichment using a Flowcomp mouse CD8 kit (Thermo Fisher Scientific), according to the manufacturer's instructions. 1*10^6 $CD8^+$ T cells were cultured with 20 IU/mL IL-2 in 6-wells flat-bottom culture plates and activated with CD3/CD28 dynabeads (ThermoFisher) or 5 μg/mL Gag-L peptide. In the case of the intratumoral $CD8^+$ T cells, they were activated by co-culturing 390.000 $CD8^+$ T cells with 180.000 irradiated B16F10 tumor cells (6000 Rad) in the presence of 1 μg/mL bsAb and 10 ng/mL IL-7 (Bio-Techne). After 24 h, supernatant from stimulated or unstimulated $CD8^+$ T cells was collected and added to BMDM cultures. For the titration experiments, a gradient of 10–100% CD3/CD28-stimulated T cell supernatant alone, or in combination with whole tumor lysate, was added to naive BMDMs for 24 h. Additionally, for the α-IFN-γ(R) conditions, T cell supernatant was pre-incubated with IFN-γ blocking antibodies (150 μg/mL, BioXCell) and BMDMs with IFN-γR blocking antibodies (150 μg/mL, BioXCell) for 1 h prior to BMDM stimulation. Alternatively, a range of 0-20 ng/mL IFN-γ (Invitrogen) was used to stimulate BMDMs in the presence LPS (100 ng/mL, Sigma Aldrich). To generate whole tumor lysate or tumor cell lysate, B16 tumors from bsAb-treated animals or RMA-Qa1$^{b-/-}$ tumors from vaccine-treated animals were processed into single cell suspensions as described above or B16F10 and RMA-Qa1$^{b-/-}$ tumor cells were harvested, combined and subjected to five free-thawing cycles in liquid nitrogen and a 37°C water bath. Cellular debris was discarded by centrifugation at 10.000RCF for 10 min and whole tumor lysate or tumor cell lysate was added to BMDMs alone, or in combination with T cell supernatant. To assess the contribution of TLR ligands and/or IFN-γ to the M1 skewing of macrophages, BMDMs were pre-incubated with a TLR4 (Tak-242, 10 μM, Tocris), TLR7+TLR9 (E6446, 200 nM, SelleckChem) or TLR1+TLR2 (Cu-CPT22, 10 μM, SelleckChem) antagonist or with IFN-γ (150 μg/mL, BioXCell) and IFN-γR (150 μg/mL, BioXCell) blocking antibodies. To block CCR5 signaling, 100 nM Maraviroc (Tocris) was added to BMDM cultures. BMDMs were stimulated for 24 h after which they were analyzed by flow cytometry or used in co-culture experiments. To assess the phagocytic and tumor cell killing capacity of macrophages, irradiated (6000Rad) RMA-Qa1$^{b-/-}$ or B16 tumor cells were pre-labeled with CFSE according to manufacturer's protocol and co-cultured with BMDMs from WT or iNOS$^{-/-}$ animals for 4 h, with an effector:target ratio of 1:4. α-CD47 with CD45.2 (RMA-Qa1$^{b-/-}$) or TA99 (B16) were added to all co-culture systems. To assess the contribution of TNF-α or NO to macrophage-mediated tumor cell death, a TNF-α-neutralizing antibody (0-500 ng/mL, Sino Biological) or the NO donor Noc18 (0-100μM, MedChemExpress) were added to the co-culture. After 4 h, cells were harvested and phagocytosis or cell death were analyzed by flow cytometry.

Griess reaction

To determine the nitrite production by macrophages, cultured BMDMs were unstimulated (M0) or pre-skewed (M1) with IFN-γ (20 ng/mL, Invitrogen) and LPS (100 ng/mL, Sigma Aldrich) for 24 h, after which culture supernatant was collected for analysis. N-(1-naphthyl)ethylenediamine and sulfanilic acid from the Griess Reagent Kit (ThermoFisher) were mixed in a 1:1 ratio to form the Griess reagent. 150μL M0 or M1 BMDM culture supernatant was mixed with 20μL Griess Reagent and 130μL deionized water and incubated for 30 min at room temperature. Absorbance of samples was measured at 548 nm in a spectrophotometer and nitrite production was determined relative to the nitrite standard solution.

L-arginine cell culture

RMA-Qa1$^{b-/-}$ and B16F10 cells were cultured in Iscove's modified Dulbecco's medium (IMDM; Invitrogen) supplemented with 8% Fetal Calf Serum (FCS; Greiner), 100 IU/mL Penicillin/Streptomycin (Gibco) and 2 mM glutamin (Gibco) at 37°C and 5% CO_2. After a confluence of 75–85% was reached, cells were harvested and counted using the Muse Cell Analyzer (Merck). 1*10^6 cells were then cultured in RPMI 1640 Medium for SILAC (L-arginine free, ThermoFisher) supplemented with 1% FCS, 100 IU/mL Penicillin/Streptomycin (Gibco) and 2 mM glutamin (Gibco) and with a dose-range from 0 to 1 g/L of L-arginine (Sigma Aldrich) at 37°C and 5% CO_2. After 48 h of culturing, cell counts and viability were determined using the Muse Cell Analyzer (Merck) and analyzed in FlowJo (Tree Star).

Quantitative real-time PCR (qRT-PCR)

Total RNA was isolated from BMDMs or sorted macrophages (Live, $CD45^+$, $CD3^-$, $CD11b^+$, $F4/80^+$) from vacc. + bsAb-treated B16 tumors, using the NucleoSpin RNA Mini kit for RNA purification (Macherey-nagel) and quantified by Nanodrop (ThermoFisher). RNA was reverse transcribed with the High-Capacity RNA-to-cDNA kit (ThermoFisher). cDNA (2.5 ng per well) was analyzed by SYBR green real-time PCR with 10 nM primers using the CFX384 Real-Time System C1000 Thermal Cycler (Bio-Rad). All primers used in this study are included in Table S3.

Quantification and statistical analysis

A Priori sample size calculation based on expected median survival times or percentages of infiltrating immune cells was used to determine the required number of animals for each experiment. Statistical significance between two groups was determined using an unpaired two-tailed Student's T test and between >2 groups using a one-way ANOVA with Tukey's correction for multiple comparisons, unless indicated otherwise. For survival analyses a log rank Mantel-Cox test and for response rates a Fisher's exact test were performed. Correlation was determined by simple linear regression or Spearman correlation for which the R, R^2 and 95% confidence interval were selected as the primary outcome parameters. All statistical tests were performed using the GraphPad Prism software (V.9). Statistical methods can be found in the figure legends or tables. Data is represented as the mean ± SEM unless stated otherwise. Statistical significance is shown as * = $p < 0.05$, ** = $p < 0.01$, *** = $p < 0.001$ and **** = $p < 0.0001$.